Photosynthesis Research
https://doi.org/10.1007/s11120-021-00838-y

REVIEW

Photophysics of nanographenes: from polycyclic aromatic hydrocarbons to graphene nanoribbons

Matthew C. Drummer[1,2] · Varun Singh[1,2] · Nikita Gupta[1,2] · Jonathan L. Gesiorski[1,2] · Ravindra B. Weerasooriya[1,2] · Ksenija D. Glusac[1,2]

Received: 5 January 2021 / Accepted: 22 April 2021

Abstract

Graphene quantum dots (GQDs) and nanoribbons (GNRs) are classes of nanographene molecules that exhibit highly tunable photophysical properties. There have been great strides in recent years to advance our understanding of nanographene photophysics and develop their use in light-harvesting systems, such as artificial photosynthesis. Here, we review the latest studies of GQDs and GNRs which have shed new light onto their photophysical underpinnings through computational and advanced spectroscopic techniques. We discuss how the size, symmetry, and shape of nanographenes influence their molecular orbital structures and, consequentially, their spectroscopic signatures. The scope of this review is to comprehensively lay out the general photophysics of nanographenes starting with benzene and building up to larger polycyclic aromatic hydrocarbons, GQDs, and GNRs. We also explore a collection of publications from recent years that build upon the current understanding of nanographene photophysics and their potential application in light-driven processes from display, lasing, and sensing technology to photocatalytic water splitting.

Keywords Graphene · Quantum dot · Nanoribbon · Polycyclic · Aromatic · Hydrocarbons · Exciton · Coherence · Diffusion · Binding energy

Introduction

Since the first isolation of single-layer graphene in 2004, there has been an explosion of studies reporting the outstanding electronic, thermal, and mechanical properties of this two-dimensional crystal (Allen et al. 2010). However, the optical properties of single-layer graphene have remained elusive because it is a semimetal with a zero bandgap (Bodenmann and MacDonald 2007). To widen the bandgap, recent synthetic efforts have been directed toward quantum confined two-dimensional nanographenes, such as polycyclic aromatic hydrocarbons (PAH), graphene quantum dots (GQDs) and graphene nanoribbons (GNRs). Since their size is smaller than the essentially infinite exciton Bohr radius of bulk graphene (Li and Yan 2010), these nanographenes exhibit tunable excitonic properties suitable for many optoelectronic applications. Optical properties of nanographenes can also be tuned using varied aromatic stability, as predicted by Clar's sextet rule (Clar 1983), or using molecular symmetry (Kastler et al. 2006; Dumslaff et al. 2016) to generate a myriad of structures with electronic transitions that span the UV, Vis, and near IR regions. These properties, combined with high mobility of free charge carriers along the nanographene axes (Morozov et al. 2008; Hong et al. 2009) have enabled the utilization of nanographenes in many optoelectronic applications, such as light-emitting diodes (Wang et al. 2017, 2020; Yuan et al. 2018, 2019a, 2020; Zhao et al. 2019; Cho et al. 2020; Pramanik et al. 2020), photovoltaic devices (Qin et al. 2015; Khan and Kim 2018; Gan et al. 2019) and photocatalytic systems (Yan et al. 2018, 2020; Tsai et al. 2020).

Given the recent growth of research articles reporting optoelectronic properties of nanographenes, we provide here a comprehensive review of fundamental nanographene photophysics and photochemistry. We anticipate that this work will complement other review articles focusing on

✉ Ksenija D. Glusac
glusac@uic.edu

[1] Department of Chemistry, University of Illinois at Chicago, 845 West Taylor Street, Chicago, IL 60607, USA

[2] Chemical Sciences and Engineering Division, Argonne National Laboratory, 9700 Cass Avenue, Lemont, IL 60439, USA

Published online: 08 May 2021

the synthesis and electronic properties of nanographenes. Specifically, photophysical nanographene studies described here are enabled by rapidly growing developments in synthetic methodologies for bottom-up synthesis of well-defined carbon structures. Several recent reports describe these advances and illustrate the richness of possible carbon and heteroatom-containing structures that can be formed using wet-chemistry reactions such as condensations, electrocyclic reactions, oxidative dehydrogenation, and many others (Narita et al. 2015; Stępień et al. 2017; Wang et al. 2019; Yano et al. 2020). Previous reviews of electronic properties in nanographenes provide information on how molecular size, shape, edge structure, and heteroatom insertion can affect the electronic conductivity and energy gaps (i.e. HOMO–LUMO gap) in these species (Rieger and Müllen 2010; Tang et al. 2013). While some of these properties are not directly related to the photophysical studies reported here, energy gap tuning is directly related to the ability to control the frequencies at which light is absorbed. Additionally, charge carrier mobilities are important in photocatalysis, where the photoinduced electron transfer to the catalytic sites form charge carriers that need to quickly migrate away from each other. Finally, previous reviews describing applications of nanographenes in sensing, light-emitting diodes, photodetectors, and photocatalysis provide insights into how fundamentally interesting excited-state properties of nanographenes can be applied in material science (Li et al. 2015a). This review summarizes the fundamental photophysical and photochemical behavior of nanographenes by building on the lessons learned from decades of research involving small PAH, such as benzene and pyrene. The excited-state behavior of PAH will be used as a platform for understanding how larger nanographenes behave and how their behavior affects their applications in material science.

Our review outlines the excited-state behavior of nanographenes, which are grouped into PAH, GQDs and GNRs (Fig. 1a). This classification is arbitrary and used here only to adhere to the terminology commonly used in the literature. For the purpose of this review, we define PAH as nanographenes with less than 13 fused rings. GQDs and GNRs are defined as nanographenes with more than 13 fused rings and differ from each other based on their shape (radiant GQDs vs linear GNRs). For brevity, non-planar nanocarbon materials, such as fullerenes, carbon nanotubes and other curved nanographenes are not discussed in this review, since the photophysics of these structures have been discussed by

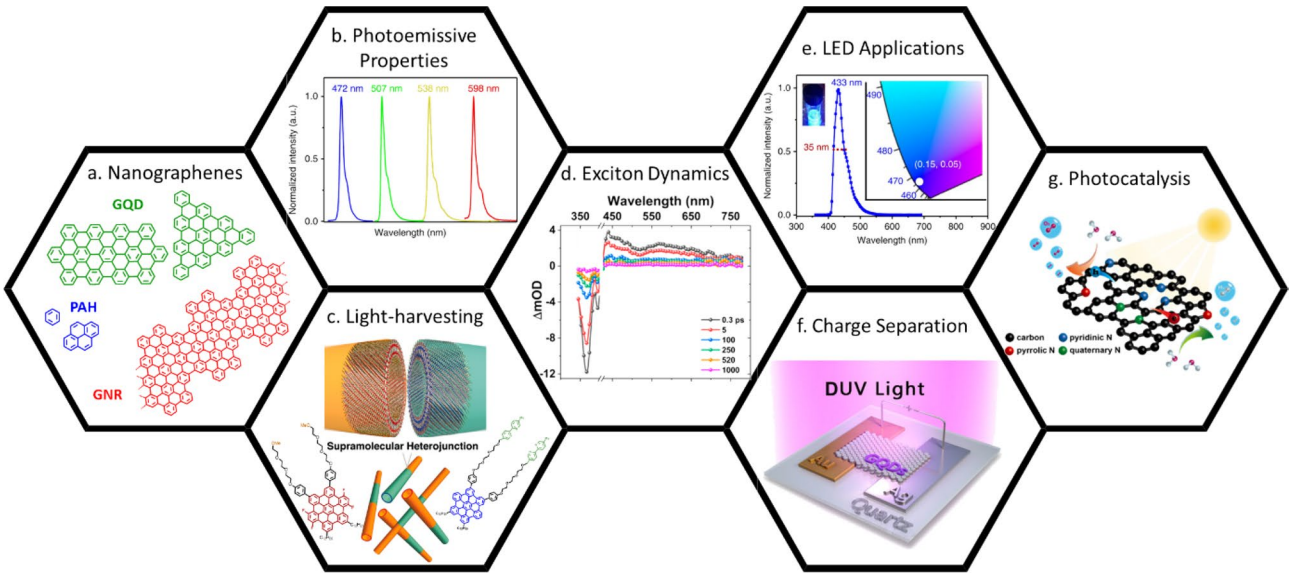

Fig. 1 **a** Structures of representative nanographenes reviewed here: PAH (blue), GQDs (green), and GNRs (red). **b** Emission spectra of four triangular GQDs of varying size (all samples were excited at 375 nm). Adapted from Ref (Yuan et al. 2018). **c** Structures of nanotubular heterojunctions, Block-NT1Cu/NT2, formed via self-assembly of hexabenzocoronene-based GQDs HBC 1 and HBC 2. Block-NT1Cu/NT2 was shown to undergo efficient excitation energy transfer across the supramolecular heterojunction using steady-state fluorescence experiments. Adapted from Ref. (Zhang et al. 2011) **d** Femtosecond transient absorption spectra for hexabenzocoronene (HBC) thin film showing decay of the signal with time representing the recombination of excitons. The sample was excited at 405 nm with pump intensity of 500 nJ per pulse with parallel polarization of pump and probe beams. **e** CIE color coordinates of conventional deep-blue carbon dot's (C-DB-CD's) and high-colour-purity deep-blue carbon dot's (HCP-DB-CD's) emission spectra. Adapted from Ref: (Yuan et al. 2020). **f** Schematic of deep-UV photodetector fabricated from a quartz substrate with Au (anode) and Ag (cathode) electrodes connected through light-absorbing, hydrothermally synthesized GQDs possessing high responsivity and detectivity. Adapted from Ref. (Zhang et al. 2015) **g** Proposed mechanistic scheme for photocatalytic CO2 reduction by a nitrogen-doped graphene quantum dot under solar illumination. Adapted from Ref: (Tsai et al. 2020)

others (Jorio et al. 2004; Dresselhaus et al. 2007; Carlson and Krauss 2008; Miyauchi 2013; Segawa et al. 2016; Soavi et al. 2016b; Dai et al. 2018; Majewski and Stępień 2019).

We begin with the *General Photophysics* section, where fundamentals of PAH excited states are described. Using simple Hückel theory, we provide a description of transitions commonly observed in the electronic spectra of PAH and the effects of symmetry and heteroatom substitution on the transition energies and oscillator strengths. This section also describes the effect of intermolecular π-interactions, which are important modulators of nanographene photophysics, particularly as the number of phenyl rings becomes large. The second section, titled *Energy Gap Tuning*, describes various methods by which electronic transitions in nanographenes are tuned by varying molecular size and shape (for example, Fig. 1b), or by insertion of heteroatoms. The third section, titled *Energy and Electron Transfer*, describes the efficiency of coherent and incoherent energy transport in nanographenes and their π-stacked assemblies (Fig. 1c,d). Furthermore, this section describes photoinduced electron transfer processes in nanographenes that contain transition metal centers. The *Applications* section provides selected examples of optoelectronic materials made of nanographenes, such as light-emitting diodes (LEDs, Fig. 1e), lasing media, photodetectors (Fig. 1f) and photocatalysis (Fig. 1g). Lastly, the *Future Directions* section provides the outlook of this field and the challenges that the nanographene community faces moving forward.

General photophysics

This section outlines the fundamental optical properties of nanographenes using simple PAH as representative examples. Since PAH are predominantly made of sp^2 carbon atoms, their UV/Vis absorption signatures are often attributed to π–π^* electronic transitions. When heteroatoms with lone pairs (such as N) are present in the aromatic framework, additional n–π^* transitions are also possible. However, these transitions are usually not relevant for the photophysics of nanographenes because they are higher in energy and lower in intensity than the π–π^* transitions. The energies of π–π^* transitions vary with the size and shape of the nanographene molecule, as we will discuss in the next section. Here, we explore how the intensities of π–π^* transitions are affected by the molecular structure. Predictions from group theory rely on the selection rules that require a nonzero transition dipole moment for allowed transitions which is achieved only if the direct product:

$$\Gamma(\psi_e) \times \Gamma(\hat{\mu}_e) \times \Gamma(\psi_{e'}) \tag{1}$$

contains the totally symmetric irreducible representation of the point group of the molecule (Harris and Bertolucci 1989). The first term, $\Gamma(\psi_e)$, is the irreducible representation for molecule in its ground state. Since most PAH have all electrons paired up in the ground state, $\Gamma(\psi_e)$ will be the totally symmetric irreducible representation of the point group of that PAH (for example, benzene belongs to D_{6h} point group, so $\Gamma(\psi_e)$ for benzene is A_{1g}). The second term, $\Gamma(\hat{\mu}_e)$, is the irreducible representation for the dipole moment operator. Since the dipole moment operator transforms the x, y, and z coordinates of the system, $\Gamma(\hat{\mu}_e)$ of the molecule can be found from the character table (in the case of D_{6h} group, A_{2u} and E_{1u} are the irreducible representations for $\Gamma(\hat{\mu}_e)$). The third term, $\Gamma(\psi_{e'})$, is the irreducible representation for the PAH in its excited state. For a totally symmetric ground state, $\Gamma(\psi_{e'})$ must be the same as one of the $\Gamma(\hat{\mu}_e)$ representations for the triple product (1) to contain a totally symmetric representation. In the case of benzene, $\Gamma(\psi_{e'})$ states can be predicted from the analysis of molecular orbitals (MOs) obtained using a simple Hückel model (Fig. 2a, b). Absorption of an ultraviolet photon by a single molecule of benzene can promote it from the ground state (S_0) to an electronically excited state (S_n). The HOMO and LUMO of benzene each consist of a pair of degenerate MOs where electron correlation interactions result in three S_0 S_n transitions which are observable as α-, β-, and p-bands in the

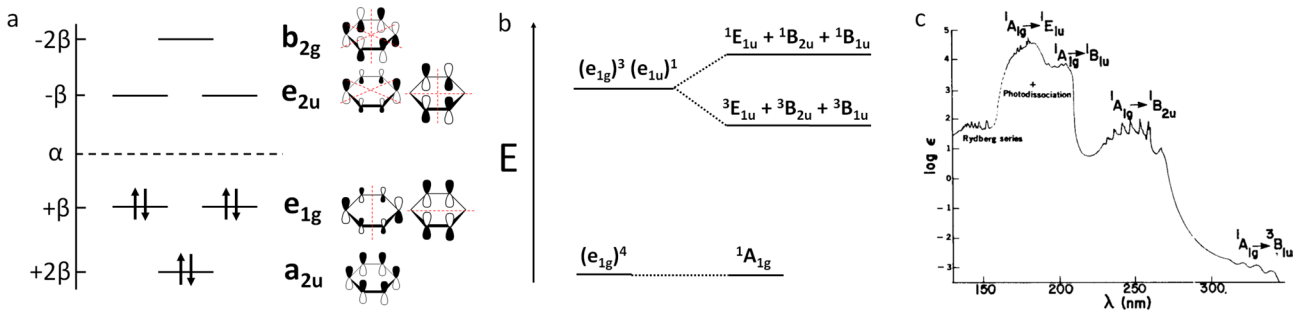

Fig. 2 **a** Molecular orbital energy diagram of benzene with bonding/antibonding structures at the side. **b** molecular orbital energy splitting in benzene. **c** UV–vis absorption spectrum of benzene (Harris and Bertolucci 1989)

UV/Vis absorption spectrum (Rieger and Müllen 2010). Del Bene and Jaffé investigated the impact of symmetry-breaking in 1968, setting the stage for the role of symmetry and non-bonding (*n*) orbitals in mono-sextet nanocarbons (Bene and Jaffé 1968). Analysis of the lowest three excited states of benzene indicates that one transition will be allowed ($^1A_{1g}$ $^1E_{1u}$) while two will be orbitally forbidden ($^1A_{1g} \rightarrow {}^1B_{2u}$ and $^1A_{1g} \rightarrow {}^1B_{1u}$). This analysis predicts the experimentally observed absorption bands of benzene well (Fig. 2c). In general, the orbitally allowed transitions exhibit extinction coefficients in the 10^3–10^5 M^{-1} cm^{-1} range, while the orbitally forbidden transitions are in the 10^0–10^3 M^{-1} cm^{-1} range (Turro et al. 2009). Here, we consider the relationship between the symmetry of benzene and its photophysical properties, namely, its energy gap (we discuss nanographene energy gaps in more detail in the next section). The allowed $^1A_{1g} \rightarrow {}^1E_{1u}$ transition in benzene occurs at an energy of 6.9 eV (~ 180 nm) while the longer wavelength $^1A_{1g} \rightarrow {}^1B_{2u}$ and $^1A_{1g} \rightarrow {}^1B_{1u}$ transitions are symmetry forbidden. The addition of a heteroatom nitrogen to the aromatic ring (pyridine) breaks the D_{6h} symmetry of benzene and increases the intensity of the forbidden transitions. Furthermore, pyridine and the diazines exhibit n–π^* transitions in the 3.3–4.3 eV range due to the interaction of the nitrogen lone pairs with the π^* acceptor MO.

As the shape of the PAH changes, the intensity of the lowest energy transition changes based on the triple product (1) discussed above. For example, anthracene and pyrene (both with D_{2h} symmetry) exhibit different intensities of their lowest energy electronic transitions due to different $\Gamma(\psi_{e'})$ values for the first excited state (allowed for anthracene and forbidden for pyrene, Fig. 3) (Turro et al. 2009). Differences in oscillator strengths of the lowest excited states also affect the fluorescence lifetimes, as predicted by relationships between the Einstein coefficients for absorption and emission: electronic transition that are allowed have intense absorption bands, but small fluorescence lifetimes and vice versa. This effect can be clearly observed in Fig. 3 showing the absorption and emission spectra of anthracene ($\varepsilon \sim 10^5$ $M^{-1}cm^{-1}$; $\tau \sim 10$ ns) and pyrene ($\varepsilon \sim 10^2$ $M^{-1}cm^{-1}$; $\tau \sim 1$ µs).

Spin–orbit coupling in PAH is generally weak, which is consistent with the small atomic numbers of their constituent carbon and hydrogen atoms. For this reason, intersystem crossing from singlet to triplet excited states in PAH generally occurs with rates of 10^6–10^8 s^{-1} (Turro et al. 2009). These values are comparable with the rate of fluorescence in PAH, so the conversion to triplet states is often observed from lowest-energy singlet excited states. Interestingly, intersystem crossing can also be observed from higher singlet excited states S_2, S_3, etc. as the nanographene size increases (Mueller et al. 2010). This behavior is associated with the so-called energy gap law derived from perturbation theory, which states that the mixing of singlet and triplet states due to spin–orbit coupling is inversely proportional to the difference in their energies, $\Delta E_{ST} = E_S - E_T$. For small PAH, the ΔE_{ST} values are usually large (up to 1 eV) which results in slow rates for triplet formation. The ΔE_{ST} value is inversely proportional to the size of the nanographene and the gap becomes as small as 0.175 eV for a GQD with diameter of 2.5 nm, resulting in triplet T_1 state generation even directly from higher singlet S_2 and S_3 states (Mueller et al. 2010).

Intermolecular interactions between nanographene molecules can drastically change their photophysical behavior. Specifically, it is well known that an increase in the nanographene surface area leads to π–π interactions between them and lower solubility (Watson et al. 2001). The origin of these π–π interactions was initially ascribed to the quadrupole moment associated with the π-electron density, but recent theoretical studies point to the dispersion forces as the leading factor for π–π interactions in large nanographenes (Grimme 2008; Martinez and Iverson 2012). Once

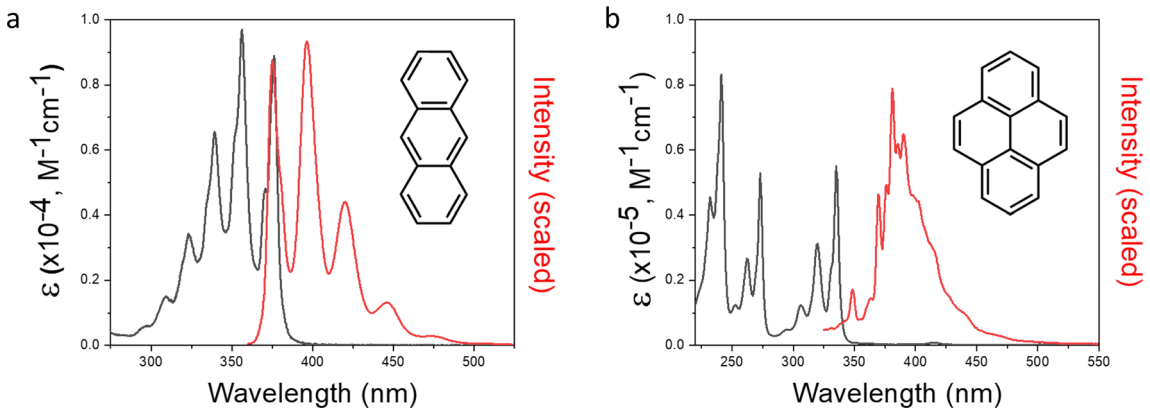

Fig. 3 Absorption (black) and emission (red) spectra of **a** anthracene ($\tau = 5.3 \pm 0.1$ ns, $\Phi = 0.36$) and **b** pyrene ($\tau = 338 \pm 9$ ns, $\Phi = 0.32$) (Berlman 1971; Nakajima 1973; Boens et al. 2007)

aggregated, the PAH chromophores no longer behave as isolated systems, but start developing new excitonic features. This effect is exemplified in the UV/Vis absorption and emission spectra of tetraazaterrylene (TAT) in dilute solution and thin crystalline film, where TAT forms π-stacked nanopillar structures (Fig. 4a, b). While TAT in dilute solution exhibits narrow bands with clear vibronic progression, the bands of the thin film are much broader, and the peaks appear at different frequencies (Yamagata et al. 2014).

To better understand the excited state photophysics of nanographene chromophores, we must consider the concept of the exciton, a quasiparticle composed of an electron–hole pair. Excitons are defined as electronic excited states that do not reside on a single chromophore, but are expressed as a linear combination of individual chromophore eigenstates. Since PAH-based π-aggregates exhibit low dielectric constants, their excitons are of the Frenkel type where photo-generated electron and hole reside on the same molecule (no charge-transfer states) (Scholes and Rumbles 2006; Cudazzo et al. 2015; Ilic et al. 2017; Tries et al. 2020). The shifts in the absorption and emission spectra of π-aggregates can be predicted using perturbation theory, where the "perturbative" interaction between the chromophores is expressed as a combination of the long-range Coulombic interactions (J_{coul}) and short-range exchange interactions (J_{CT}) (Hestand and Spano 2017). Long-range coupling (J_{coul}) is associated with the interactions between transition dipole moments of individual chromophores and has been successfully used to describe the red- and blue-shifts in the electronic transition energies of J and H aggregates of many organic chromophores (Fig. 4c). The short-range exchange coupling (J_{CT}) is associated with Dexter-type electron transfer between individual chromophores and can be modeled as a charge-transfer, state-mediated process (Fig. 4d). The additive contributions of J_{coul} and J_{CT} terms are needed to describe the complicated spectral changes associated with π-stacked PAH chromophores and this model has been shown to successfully reproduce the experimental spectra of TAT (Yamagata et al. 2014).

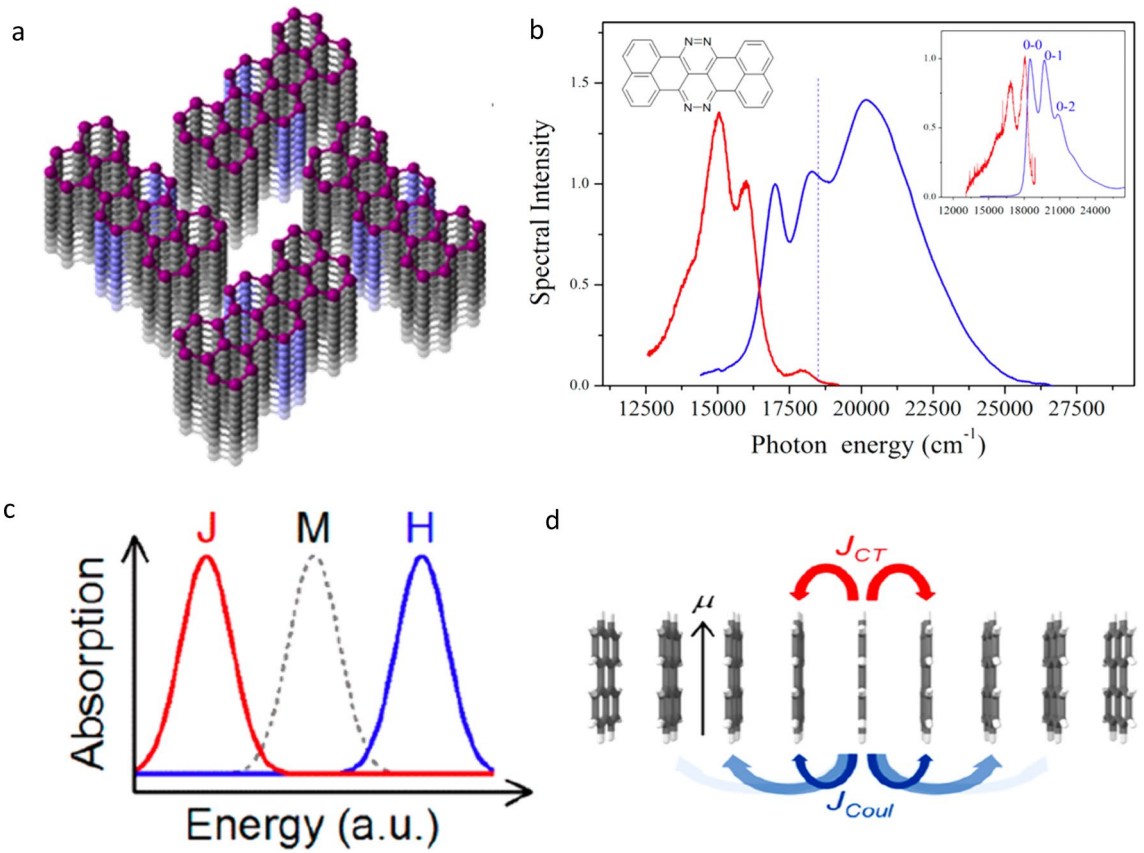

Fig. 4 **a** Crystal structure of 7,8,15,16-tetraazaterrylene (TAT) aggregates, **b** Absorption (blue) and emission (red) spectra of TAT (inset; spectra of 100 nM solution of TAT in chloroform), **c** Ideal absorption spectra for J- and H-aggregates, **d** Model of short-range, charge-transfer-mediated interactions, J_{CT}, and long-range Coulomb interactions, J_{coul} (Yamagata et al. 2014; Hestand and Spano 2017)

Energy gap tuning

When other structural parameters (edge-structure, symmetry, chemical functionalization, etc.) are held constant, there exists an inversely proportional relationship between the size of a nanographene and the magnitude of its energy gap. For example, theoretical analysis of zig-zag and armchair GQDs has shown that the energy gap in GQDs falls off with $1/N$, where N is the number of hexagonal units along the edge of the GQD (Zhang et al. 2008). Similar behavior was observed for GNRs, where the gap was found to fall off $1/w$, where w is the width of the nanoribbon (Fig. 5a, b) (Son et al. 2006). However, the exact relationship between GNR width and energy gap is a bit more complicated than this. Armchair-GNRs can be grouped into different subfamilies with $N_a = 3p$, $3p+1$, and $3p+2$, where N_a is the number of dimer lines (d_a) across the width of the GNR and p is an integer (Fig. 5c). The energy gaps of these families of GNRs follow the trend $3p+2 < < 3p < 3p+1$ (Son et al. 2006). Regarding zig-zag GNRs, the relationship between energy gap and ribbon width appears to follow the simple inversely proportional relationship just described (Fig. 5d).

Recent developments in the bottom-up synthesis of nanographenes (Huang et al. 2018; Zhao et al. 2018; Singh et al. 2020b) have enabled the synthesis and spectroscopic investigation of well-defined molecules and the results of these experiments generally confirm the theoretical predictions. It has been demonstrated that the energy gaps of fully benzenoid PAH decrease from 3.9 eV in triphenylene (a 4 fused-ring PAH) to 2.2 eV for a larger, 15-ring GQD (Rieger and Müllen 2010). This relationship has been demonstrated for a wide variety of PAH and GQDs that take on many different morphologies. For example, triangular-GQDs (T-GQDs) exhibit a progressive redshift in absorbance and emission peaks with increasing size (Yuan et al. 2018). GQDs of other shapes, such as hexa-*peri*-hexabenzocoronene (HBC) derivatives, have the same inversely proportional relationship between their sizes and optical gaps (Zhang et al. 2015). Systematic energy gap engineering in GQDs via extension of the conjugated π-system (by

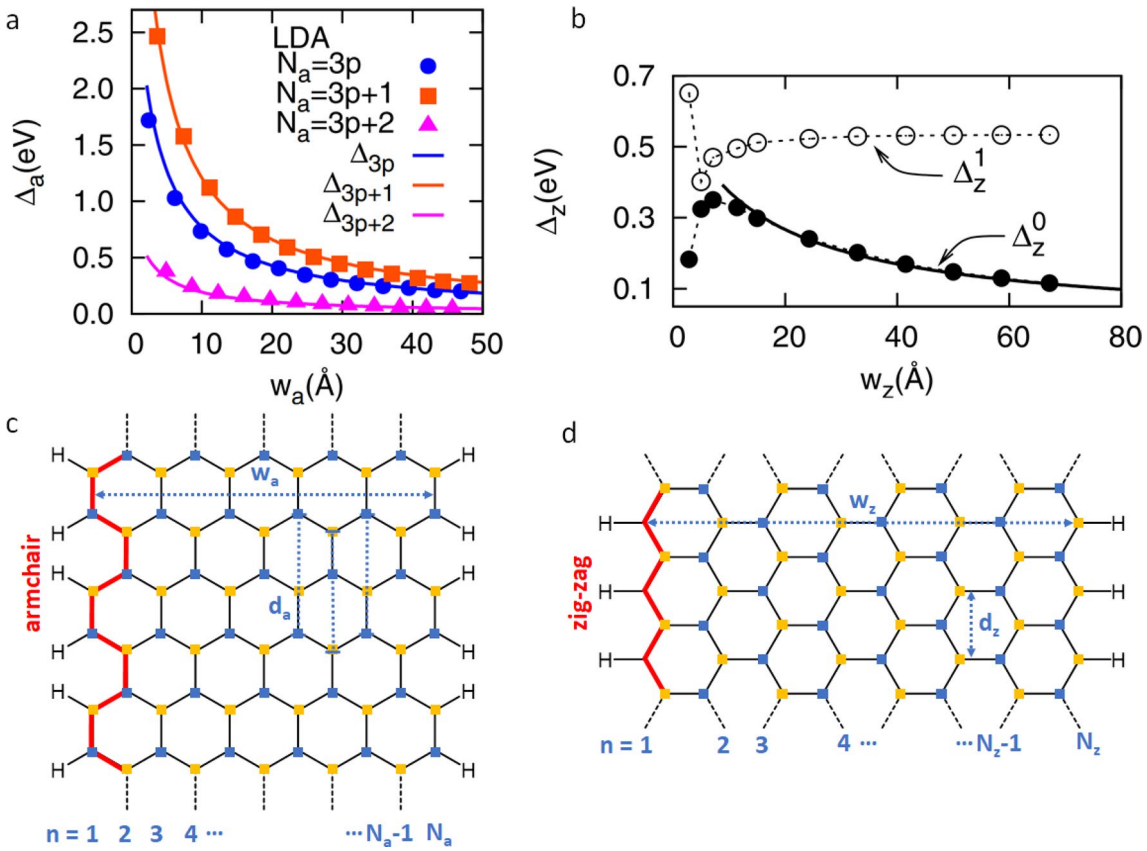

Fig. 5 **a** Energy gap as a function of GNR width where N_a is the number of dimer lines (d_a) across the ribbon width and p is an integer. **b** Bandgap (Δ^0_z) and energy splitting (Δ^1_z) of zig-zag GNRs as a function of ribbon width. **c** Representative structure of an armchair GNR where w_a is the width and d_a is the 1D unit cell distance. Characteristic armchair edge is highlighted in red. **d** Representative structure of a zig-zag GNR where w_z is the width and d_z is the 1D unit cell distance. Characteristic zig-zag edge is highlighted in red (Son et al. 2006)

solvothermal condensation with aromatic ligands) has been shown to stabilize the π^* acceptor MO energy resulting in a narrowing of the energy gap by 0.52 eV (Yan et al. 2018). Energy gap tuning in GNRs is accomplished using similar strategies. Narita and coworkers demonstrated the length-dependent quantum confinement effect in GNRs in a 2013 study which shows a red-shift absorption band as the nanographene increases in length from dimer to trimer to nanoribbon (Narita et al. 2014).

Nanographene edges play a significant role in the energy gap as well (Yamijala et al. 2015; Ivanov et al. 2017; Dumslaff et al. 2020). The size dependence presented in Fig. 5 shows that the energy gap in GQDs falls off more drastically with *N* if the edges are zig-zag. Similarly, zig-zag GNRs exhibit smaller gaps than armchair GNRs of similar size. This behavior can be readily described using the simple and chemically intuitive Clar's sextet rule (Solà 2013), which states that the stability of a given PAH is proportional to the number of benzene-like π-sextet moieties that it contains. For example, triphenylene is much more stable than tetracene (Fig. 6a, b). Similarly, larger nanographenes with armchair edges have more π-sextets than those with zig-zag edges (as exemplified for triangular GQDs in Fig. 6c, d. Additionally, zig-zag PAH contain more nodes than armchair PAH. The presence of these nodes destabilize the HOMO level which narrows the energy gap (Yamijala et al. 2015). The increased stability of PAH is associated with large energy gaps, explaining the trends observed in Fig. 5 and the UV/Vis absorption spectra in Fig. 6 (Yamijala et al. 2015).

Clar's sextet rule can also be used to explain the dependence of the energy gap on the shape of the nanographene (Rieger and Müllen 2010). For example, triphenylene and tetracene are both 4-ring (18 carbon atoms in total) PAH. However, triphenylene contains three Clar's sextets while tetracene contains only one (see Fig. 6a, b), which results in tetracene exhibiting lower energy absorption than triphenylene as well as higher reactivity. Nanographene symmetry can also be used to tune the energy gaps. For example, Müllen and co-workers investigated a series of HBC-derivatives synthesized to have different symmetries (D_{6h}, C_{2v}, D_{2h}, *and* D_{3h}) (Kastler et al. 2006; Dumslaff et al. 2016).

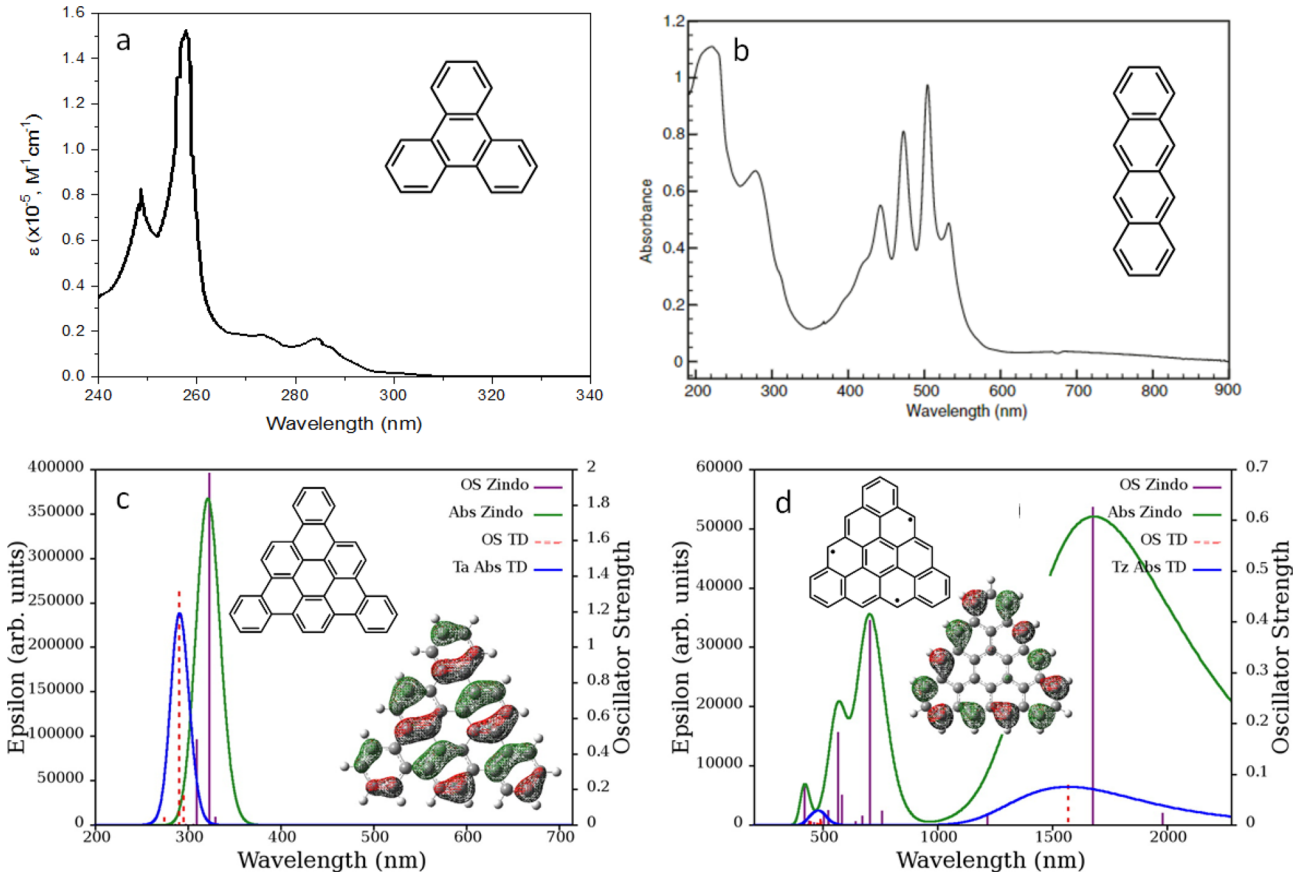

Fig. 6 **a** Absorption spectrum of triphenylene with structure in inset. **b** Absorption spectrum of tetracene (film deposited on a MgF_2 disk) with structure in inset. **c** Calculated absorption spectrum of an armchair T-GQD, inset shows Clar's sextet structure (top) and calculated HOMO isosurface (bottom). **d** Calculated absorption spectrum of a zig-zag T-GQD, inset shows Clar's sextet structure (top) and calculated HOMO isosurface (bottom) (Talrose et al. (2020); Bryson et al. 2011; Yamijala et al. 2015)

The authors found that higher symmetry GQDs (such as D_{6h}) exhibit narrow UV/Vis bands with few transitions and broader photoluminescence (PL) spectra compared to lower symmetry PAH (such as C_{2v}). Reduction in symmetry leads to more allowed transitions and, consequently, broader and less featured UV/Vis spectra and similar shape-dependent behavior was observed in other nanographenes (Rieger and Müllen 2010; Stępień et al. 2017).

Edge functionalization is another strategy for tuning the energy gaps of GQDs due to the charge transfer effects of electron donating and withdrawing groups (Bao et al. 2011; Wang et al. 2016; Hai et al. 2018; Yuan et al. 2018). Yun Li et al. carried out a computational study on the electronic and optical properties of GQDs edge-functionalized with $–NH_2$, –OH, –F, –CHO, $–COCH_3$, and –COOH groups (Li et al. 2015b). Density functional theory (DFT) calculations of C=O functionalized GQDs predict the lowering of HOMO and LUMO energy levels due to the π-electrons in C=O that can extend the π-electron system in the GQD moiety. Amino groups may also tune the optical properties of GQDs, but their influence on the energy gap is much weaker due to the cancellation of the frontier orbital hybridization effect by larger charge transfer effects. Yuan et al. demonstrated the importance of amination by comparing the optical properties of aminated and non-aminated GQDs where the aminated analogs exhibited a larger emission full-width at half-maximum (FWHM) of 62 nm, possessed a bandgap of 2.96 eV, and quantum yield (QY) of 70% (Yuan et al. 2020). The promising results of aminated GQDs is attributed to the reduced defects in the GQD structure which significantly reduces non-radiative pathways. It should also be noted that amination reduces the symmetry of GQDs which manifests in the red shifted calculated absorption and emission spectra (Wang et al. 2016). Furthermore, tailoring electron-donating groups to the peripheries of GQDs results in the creation of non-bonding (n) orbitals that lay higher in energy than the π donor MO of the GQD, but lower in energy than the π^* acceptor MO, which has narrowed the gap of coal-derived GQDs from 2.40 eV to 1.94 eV (Yan et al. 2020). Conversely, electron withdrawing groups can reduce the energy gap in GQDs as demonstrated by the 100 nm emission wavelength red shifting of chlorine atom (Cl) functionalized GQDs (Zhao et al. 2018).

Energy gap tuning has also been demonstrated by introducing heteroatoms to the sp^2 carbon framework of GQDs and GNRs, such as B, N and O atoms (Dou et al. 2012; Cloke et al. 2015; Kawai et al. 2015, 2018; Tsai et al. 2020). For example, the introduction of boron atoms into GQDs results in significant energy lowering of the absorption and emission bands (Fig. 7a, b) (Dou et al. 2012). The corresponding DFT calculations show that the observed lowering of electronic transition energies is associated with the significant contribution of boron 2p orbitals to the frontier orbitals of the GQD (Fig. 7c). Similarly, the optical gap of GQDs have been controllably altered from 2.31 eV to lower energies such as: 2.18 eV for N-doped, 2.12 eV for S-doped, and 2.04 eV for N,S-doped GQDs (Yan et al. 2020). The location of nitrogen heteroatoms in the GQD flake (pyridinic

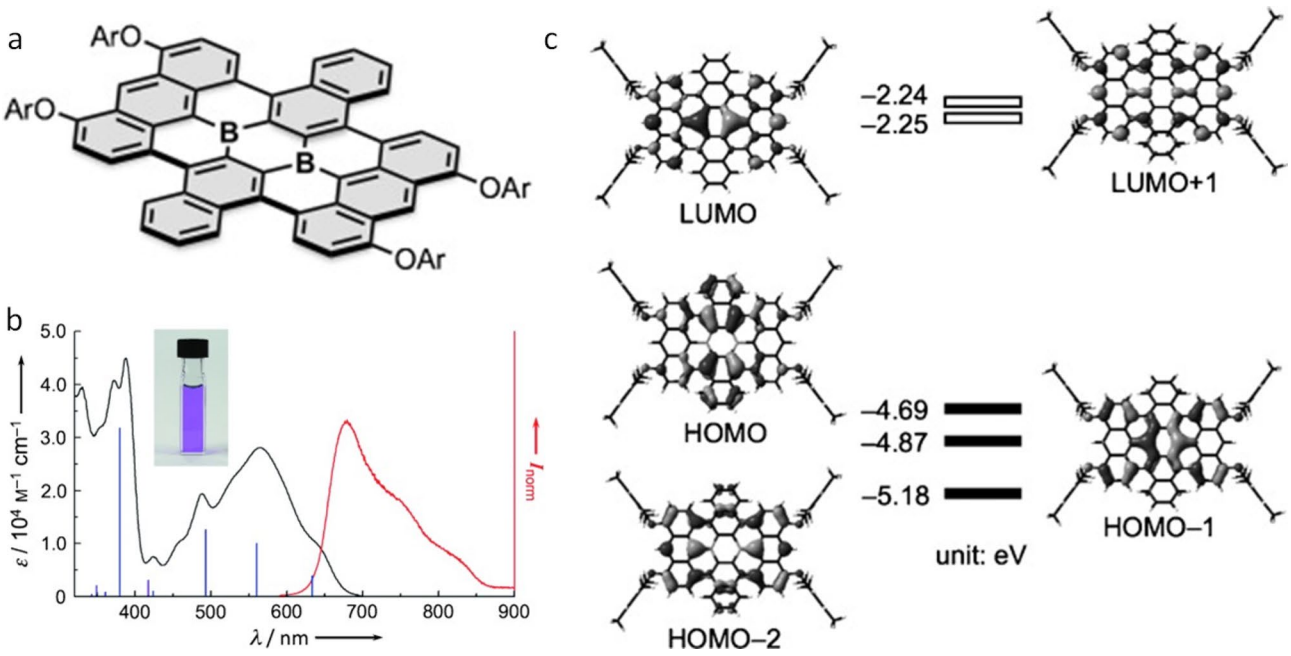

Fig. 7 **a** Structure of a boron heteroatom-containing PAH (B-PAH). **b** Measured UV–vis absorption (black) and emission (red) spectra of B-PAH **c** Calculated MO energies of B-PAH (Dou et al. 2012)

edge, pyridinic center, pyrrolic, graphitic, or amine) also plays a role in the energy gap where it has been reported that amines tend to red-shift GQD emission whereas pyridinic nitrogen atoms tend to blue-shift it (Calabro et al. 2019; Tsai et al. 2020).

Energy and electron transfer

Electronic excitation energy transport in nanographenes has been explored for two types of systems. One involves intramolecular excitation transfer along the covalently linked framework of a single nanographene (such as GNR) and another involves intermolecular assembly of nanographenes (such as π-stacked GQDs). These covalent and π-stacked architectures are multi-chromophore systems: GNRs are defined as covalently linked arrays of chromophores, where each chromophore is spatially located on a single monomeric unit, while GQD assemblies are an array of GQD chromophores held together by van der Waals interactions. Electronic excitation transport between these chromophores can be either coherent or incoherent, depending on the degree of electronic coupling between the chromophores. If the coupling is strong, excitonic states are formed, where the coherent superposition of resonating excited states allows for energy transfer within the exciton size (Olaya-Castro and Scholes 2011). Probability amplitudes on the donor and acceptor sites of such excitonic states describe coherent energy transfer. Unfortunately, exciton coherence lengths are generally small in organic chromophore assemblies at room temperature, due to the random vibrations induced from the environment that lead to exciton decoherence and reduced role of coherent energy transport in excitonic materials. The energy transfer between weakly coupled chromophores is described by an incoherent hopping (Förster type) mechanism, in which the excitation is localized on one chromophore unit and is transferred to another unit via the "inductive resonance" mechanism that does not require the orbital overlap between donor and acceptor sites. If the orbital overlap between the chromophores exists, the energy transport can also occur via Dexter-type mechanism, in which the excitation is transferred by coupled electron and hole transfers between the donor and acceptor chromophores. Incoherent energy transfer processes are dominant in these systems. Recent studies that report coherent and incoherent energy transport in nanographenes are discussed below.

Only a handful of studies reporting exciton coherence lengths (or exciton size; the number of chromophores over which the exciton is delocalized) in nanographenes can be found in the literature. In some cases the estimate of exciton size can be obtained from steady-state emission spectra (Spano and Yamagata 2011) by investigating the relative intensities of the 0–0 and 0–1 vibronic bands of the emission spectra. The idea behind this treatment is that at T = 0 K, the I^{0-0} is directly proportional to exciton size, while the intensity of the 0–1 vibronic progression is relatively insensitive to exciton size. This effect can be observed in the emission spectra of tetracene crystals shown in Fig. 8 (Lim et al. 2004). As the temperature increases, the I^{0-0}/I^{0-1} ratio decreases, as the exciton size becomes smaller due to thermally induced disorder and loss of degeneracy among the chromophore eigenstates. The modeling of experimental emission spectra provided a low-temperature exciton size estimate of ~ 9 molecular units in tetracene crystals. In a study by Moran and co-workers, exciton size in tetracene and rubrene crystals was determined using low-temperature

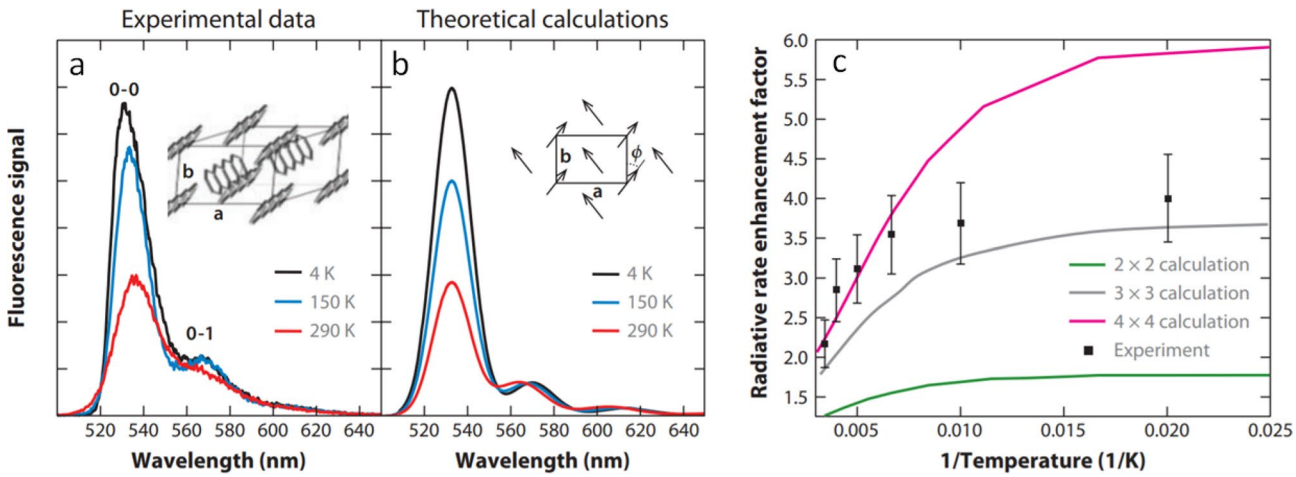

Fig. 8 **a** Temperature-dependent emission spectra of tetracene integrated over the first 200 ps (left) and simulated emission lineshapes of tetracene at different temperatures with fixed exciton size of 9 tetracene molecules (right). Growth of 0–0 peak at lower temperatures indicates an increase in singlet exciton coherence length. **b** Radiative rate enhancement as a function of temperature, measured by the amplitude of the initial fluorescence signal (Lim et al. 2004)

linear absorption spectroscopy and model calculations. The calculations showed concentration of the oscillator strength on the lowest energy transition which is a well-known signature of exciton delocalization. The exciton size was found to be ~ 18 molecular units for tetracene and rubrene crystals at 200 and 78 K, respectively (West et al. 2010). In a subsequent study, Moran and coworkers determined exciton size of ~ 16 molecular units in perylene crystals at 78 K using low temperature linear absorption spectroscopy and model calculations (West et al. 2011). While studies listed above investigate PAH crystals, recent studies have explored exciton coherence lengths for nanographenes and their 3D assemblies. For example, a recent study investigated exciton size in two topologically different pyrene-containing Zr-based metal–organic frameworks (MOFs) (Yu et al. 2018). In this work, exciton coherence lengths were evaluated computationally, using transition density matrices derived from time-dependent DFT. The results indicate that the excitons are delocalized over four pyrene chromophores in these systems and that the delocalization depends on the interchromophore separation in MOFs with different morphologies.

Our group recently explored 1D π-stacked assemblies of GQDs using transient absorption spectroscopy and DFT calculations (Fig. 9) (Singh et al. 2020b). Experimental determination of exciton size utilizes the fact that the ground-state bleach in the transient absorption signal directly reports the number and size of excitons formed by the pump beam. By measuring the bleach signal at early times after the excitation pulse as a function of pump fluence, the exciton size in two different GQD assemblies were evaluated to be 1–2 monomer units (Fig. 9a, b). Our result was consistent with the exciton sizes calculated using the one-particle transition density formalism, where exciton size of 2 molecular units were obtained. Our results indicate very small exciton delocalization on one-dimensional aggregates. Even if the exciton size is large at the Frank–Condon point, the decoherence is generally fast and excitons generally "self-trap" on picosecond timescales (Sung et al. 2015; Kaufmann et al. 2018), providing further evidence that the coherent energy transport in these systems is not significant. While exciton size of GNRs has been explored much less, studies comparing the absorption spectra of oligomers with varying length indicate that the excitons delocalize over no more than four monomer units (Huang et al. 2018).

Incoherent energy transport (exciton diffusion length) in chromophore assemblies can be measured using various techniques such as exciton-exciton annihilation, quenching techniques and Förster resonance energy transfer (FRET) and each technique have their own advantages and disadvantages (Lin et al. 2014). Steady-state and time-resolved surface quenching techniques require steady-state or time-resolved PL measurements to determine exciton quenching in bilayers of chromophore and quencher such as C_{60} fullerene. The exciton diffusion length is estimated from the PL

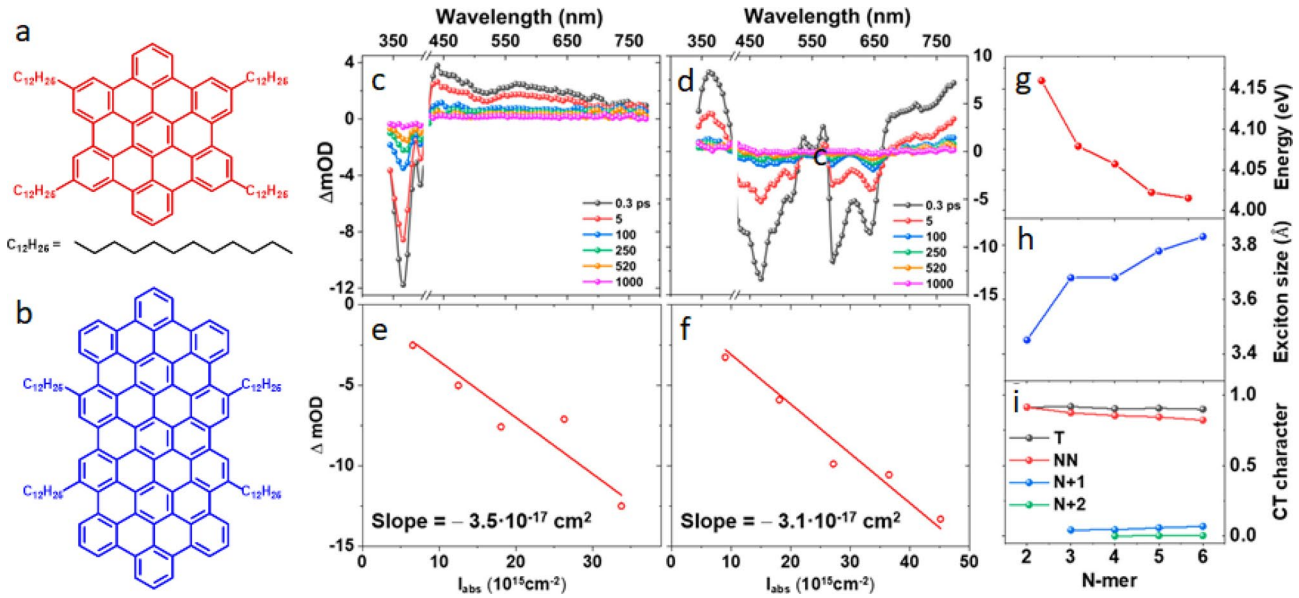

Fig. 9 Structures of alkylated **a** HBC and **b** CQD. Transient absorption spectra for **c** HBC and **d** CQD thin films in poly(methyl methacrylate) matrix. Samples were excited at $\lambda_{exc} = 405$ nm, and pump intensity was at 500 nJ per pulse with parallel pump and probe beam polarization. Circles represent ΔA_{ani} (t = 0) values obtained by probing at 367 and 467 nm [for HBC **e** and CQD **f,** respectively] as a function of the absorbed pump intensity, I_{abs}. Solid lines present the fitting model. **g–i** Results from the DFT calculations on the exciton size in oligomers of the HBC model: dependence of the **g** lowest charge-transfer exciton energy, **h** size, and **i** charge-transfer character on the oligomer size N (T = total, NN = nearest neighbor, $N+1$ = neighbor + 1, and $N+2$ = neighbor + 2) (Singh et al. 2020b)

measurements of the chromophore layer of different thickness with and without quencher layer. Bulk quenching with Monte Carlo simulations is another technique to determine exciton diffusion parameters. Here, the chromophore with increasing concentrations of the quencher is blended and the PL lifetimes are added to the Monte Carlo simulation which provides exciton diffusion parameters. The exciton diffusion coefficients can also be determined by FRET from the spectral overlap between absorption and emission spectra of the chromophores. The exciton-exciton annihilation technique operates on the principle that at high excitation densities, two excitons can interact and annihilate with each other within their lifetime. A loss in the rate of exciton decay is observed as a function of excitation intensity and diffusivity of the excitons which can be modeled to extract exciton diffusion parameters. The article by Nguyen and coworkers (Lin et al. 2014) studies the exciton diffusion length in organic semiconductors by six different experimental techniques and a very good agreement was found. Also, semicrystalline materials gave higher exciton diffusion coefficients when measured using exciton-exciton annihilation. One-dimensional π-assemblies of PAH, such as perylene bisimide stacks, have been studied extensively and an exciton diffusion length of up to 96 nm was observed using the exciton-exciton annihilation method (Marciniak et al. 2011). Our group has also explored exciton diffusion parameters for two GQD assemblies using exciton-exciton annihilation approach and diffusion length of 16 and 3 nm were found, respectively (Fig. 9). Here we observed two types of excitons: mobile and immobile, where the immobile excitons were formed due to trapping of the mobile excitons, likely caused by torsional motion of the molecules in the aggregate structure (Singh et al. 2020b).

Excitons in nanographene materials exhibit exciton binding energies (E_b) that are much larger than the available room temperature thermal energy ($k_bT \sim 26$ meV), resulting in low efficiency of spontaneous exciton dissociation into free charge carriers. Theoretical studies have shown that E_b's are closely related to the exciton size in GNRs, which are in turn directly related to the GNR width w (Zhu and Su 2011). Figure 10 shows that the binding energies range from ~ 450 meV for wide GNRs to ~ 2.5 eV for narrow GNRs. Interestingly, the dependence of E_b (and exciton size) on the GNR width follows the same trend as the energy gap discussed earlier. For the same GNR width, the $3p+2$ family exhibits smaller E_b values than the member of the $3p$ family. Similar computational studies have been performed for GQDs where many-body effects (interactions between electron and hole) in confined systems are taken into account to yield a quasiparticle gap which is used in the calculation of E_b. For example, Wang et. al. produced a computational study on GQDs of varying size and edge and report E_b values larger than 1 eV, which are expected and larger than E_b's in carbon nanotubes and GNRs due to the higher degree of quantum confinement in GQDs. The authors also report that, generally, GQDs exhibit a decrease in E_b as the lateral size of the GQD increases, with exceptions to this rule stemming from symmetry effects as discussed earlier in this review (Li et al. 2015c).

Experimental E_b values in GNRs confirm computational predictions discussed above. For example, E_b has been determined for 1.7 nm wide GNR **23** (Scheme 1) using ultrafast THz spectroscopy (Tries et al. 2020). Using 40 fs laser pulses, the excitons and/or charge carriers are generated along the GNRs. Then, a THz probe beam is used to distinguish between excitons and free carriers, based on the different response that these species exhibit in the frequency-resolved conductivity. When a low-energy pump beam is used (1.63 eV), only excitonic states are formed (Fig. 11). However, when a higher energy pump beam is used (3.1 eV) charge-carriers are formed. By varying the energy of the pump-beam, the authors found that $E_b = 700$ meV, which is similar to the theoretically calculated value of 550 meV. The authors further investigated the dynamics of charge carriers and excitons in GNRs and found that charge carriers recombine quickly to form excitons (0.8 ps), while exciton lifetimes are relatively long-lived (> 100 ps). Exciton binding energy of a GNR (**21** in Scheme 1) was determined computationally using the ab initio GW plus Bethe–Salpeter (GW-BS) method. The binding energy is determined by taking the

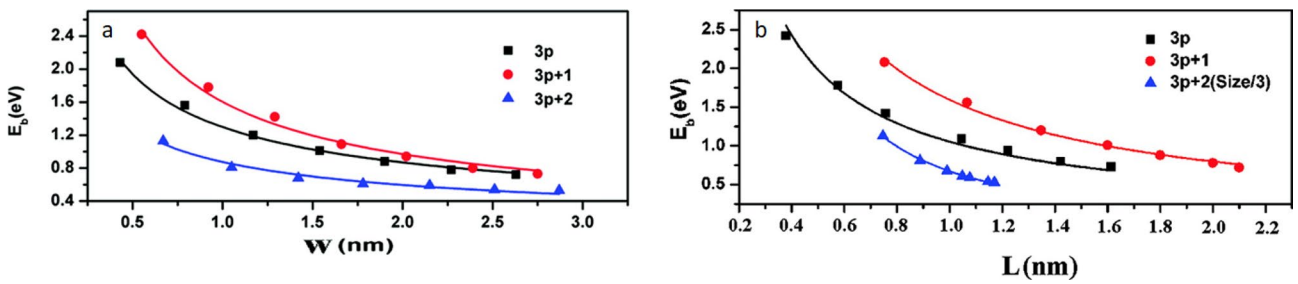

Fig. 10 **a** Exciton binding energy, E_b, as a function of GNR width, w. **b** Exciton binding energy as a function of exciton size, L (Zhu and Su 2011)

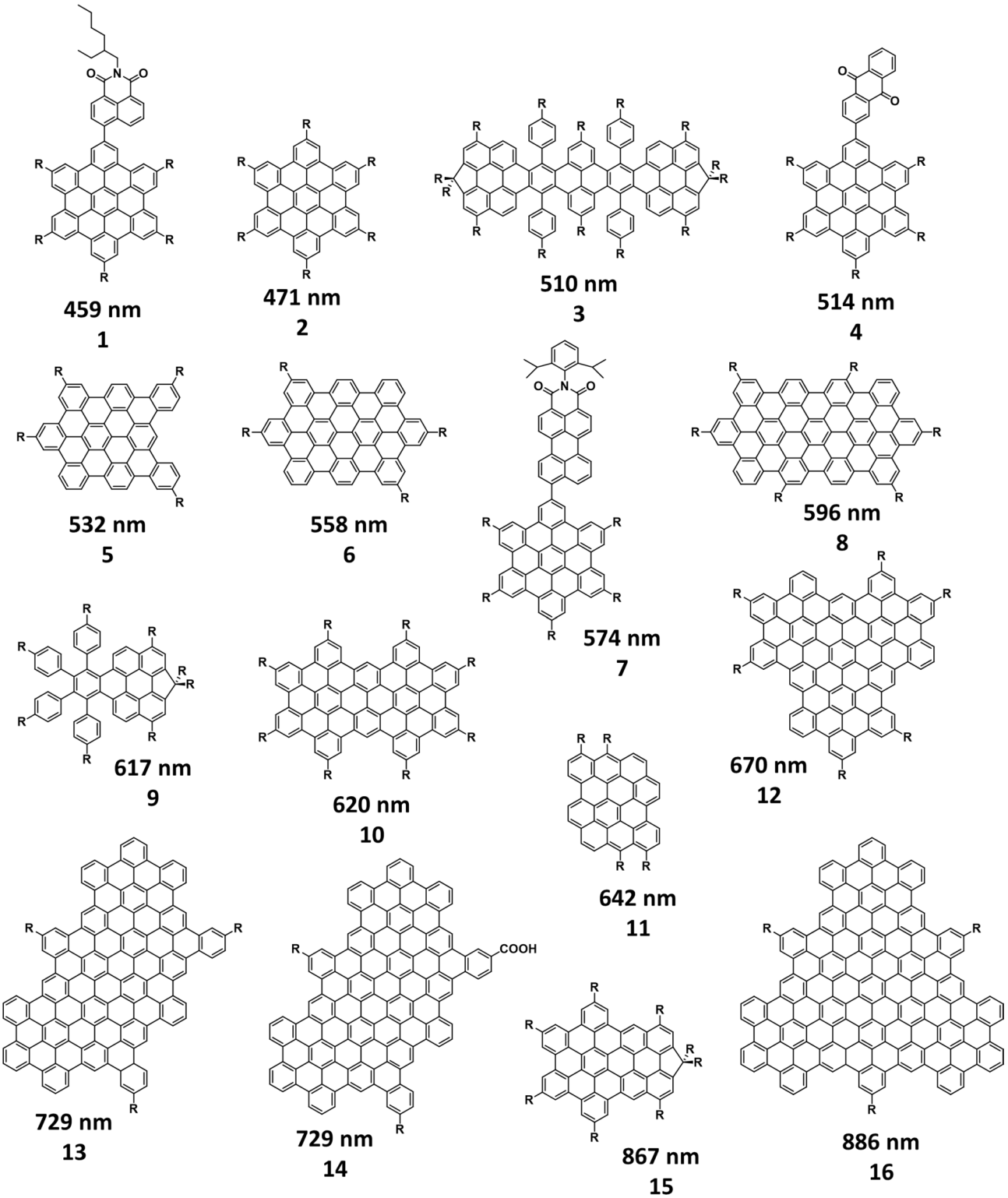

Scheme 1 Energy gaps for an assortment of **(1–16)** GQDs and **(17–26)** GNRs, reported in units of photon wavelength. Exciton binding energy, E_b, is reported for selected structures (Yan et al. 2011; Jensen et al. 2013; Narita et al. 2014; Denk et al. 2014; Sun et al. 2015; Soavi et al. 2016a, b; Keerthi et al. 2016; Chen et al. 2017; Paternò et al. 2017; Deilmann and Rohlfing 2017; Zhu et al. 2018; Hu et al. 2018; Huang et al. 2018; Ji et al. 2019; Xu et al. 2019; Han et al. 2020; Tries et al. 2020; Zou et al. 2020)

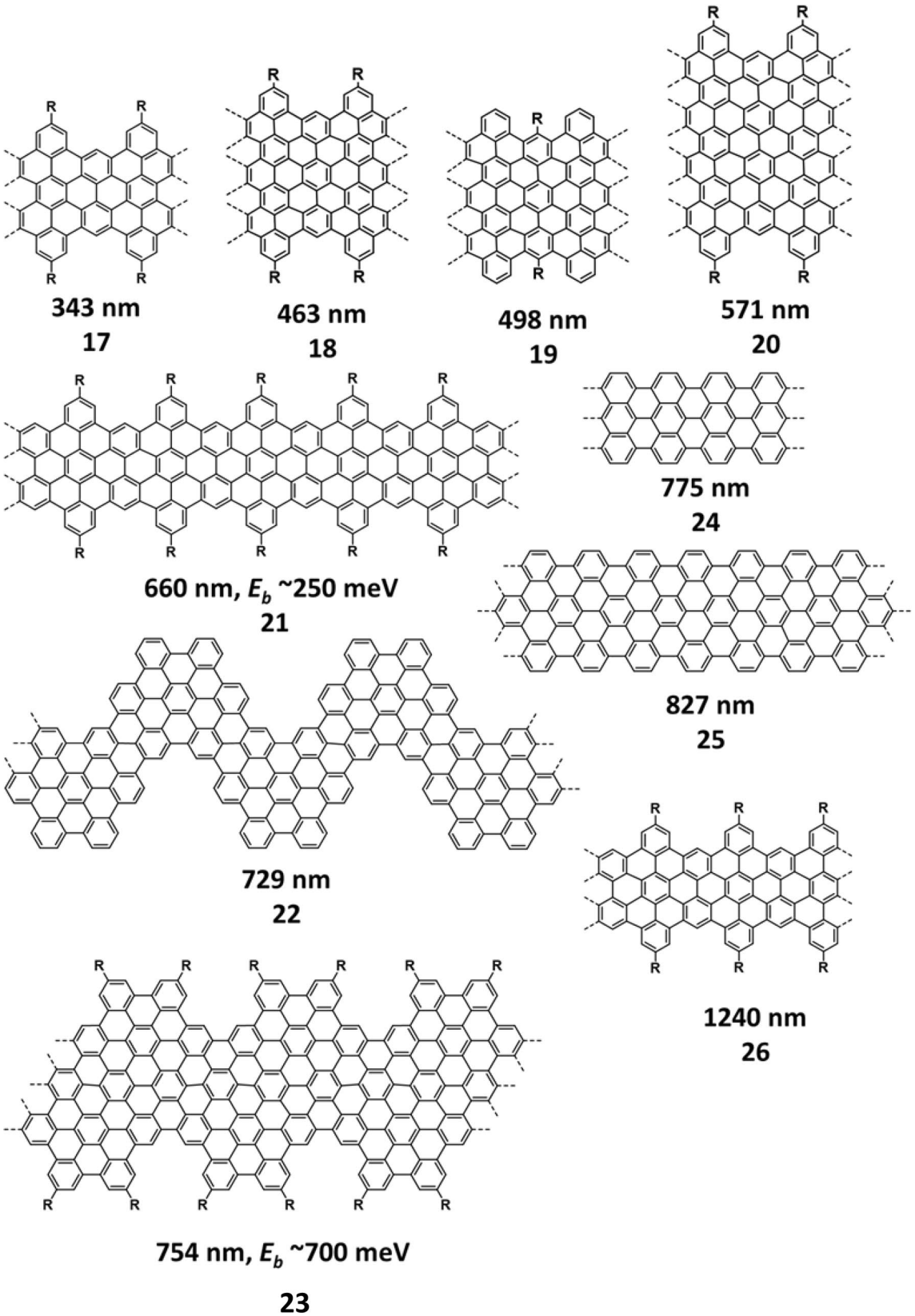

Scheme 1 (continued)

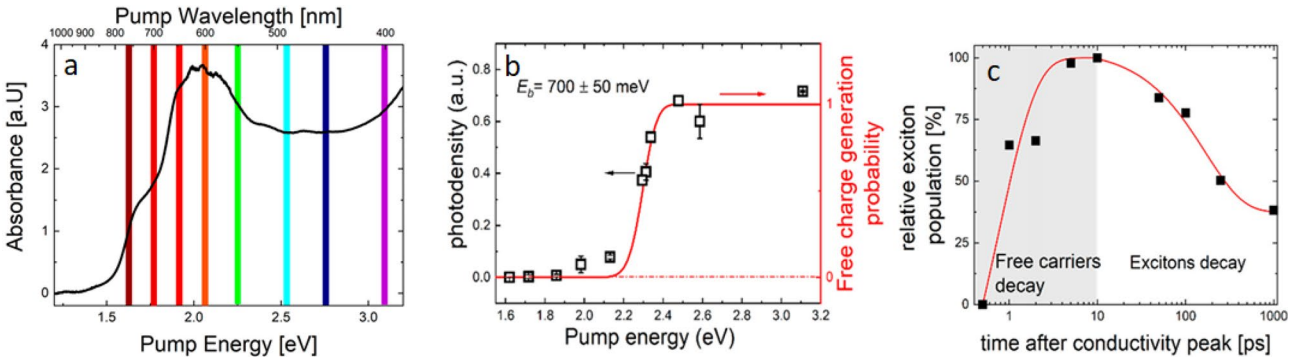

Fig. 11 **a** UV–vis absorption spectrum of GNR **23** with excitation wavelengths highlighted in color. **b** Maximum of real conductivity signal as a function of excitation photon energy. The signal sharply rises when the exciton is dissociated into free charge carriers. **c** Time profile for the rise and decay of the real conductivity signal (free carrier response) and decay of the imaginary conductivity signal (exciton response) (Tries et al. 2020)

difference between the GW quasiparticle bandgap and the GW-BS excitonic transition energy. The resulting giant binding energy was found to be ~ 1.5 eV, consistent with what is expected for excitons in GNRs (Soavi et al. 2016a). Here, the same approach was used to computationally determine the exciton binding energy in another GNR (**24** in Scheme 1). The binding energies for the E_{11} and E_{22} excitations (lowest energy, allowed excitonic transitions) were reported as 1.8 and 1.4 eV, respectively, and correspond to quasi-1D excitons that are fully delocalized along the GNR width and spatially distributed along the ribbon axis (Denk et al. 2014). GNR **24** deposited on an Au(111) surface exhibits a decrease in exciton binding energy from 1.8 to 0.160 ± 0.060 eV due to substrate polarization effects and strong electronic coupling between the GNR and gold substrate (Bronner et al. 2016).

Surprisingly, the experimentally obtained E_b values for GQDs are significantly lower (0.1–0.6 eV) (Yuan et al. 2018, 2020; Ji et al. 2019) than those predicted by theory (~ 1.2 to 1.9 eV) (Li et al. 2015b, c). For example, E_b values for two types of GQDs were obtained using temperature-dependent PL lifetimes (at higher temperatures, thermal energy from the environment causes excitons to dissociate into charge carriers, resulting in shorter PL lifetimes) and the values in the 100–150 meV range were obtained (Yuan et al. 2018, 2020). Somewhat larger values were obtained for indium-doped tin oxide (ITO)-tethered GQDs, where E_b was determined using spectroelectrochemical methods (Ji et al. 2019). The reasons for the observed mismatch could be associated with the experimental techniques used in these studies. Specifically, the PL lifetime method assumes that the lifetime decrease is associated with the exciton dissociation into charge carriers, which may not be the case. A more accurate analysis would involve the direct detection of charge carriers using THz spectroscopy.

Electron transfer from photoexcited GQDs to transition metal-based semiconductors has been investigated previously by several groups (Manga et al. 2009; Elliott et al. 2016; Long et al. 2017; Shan et al. 2019; Han et al. 2020; Yan et al. 2020; Singh et al. 2020a). Generally, two types of hybrid structures have been explored, where one involves GQDs attached to the surface of metal oxide nanoparticles (SnO_2 or TiO_2) and another is related to 0D/2D van der Waals heterojunctions composed of zero-dimensional GQDs and two-dimensional MoS_2 or graphene. In all studies, the effect of GQD size on the dynamics of photoinduced electron transfer has been explored. All studies indicate that the hot electron injection takes place from photoexcited GQDs. For example, Fig. 12a shows the time-resolved second harmonic generation (SHG) signal, which is proportional to the number of charges that are photogenerated, measuring the electron transfer from excited GQD to TiO_2. The growth of the signal occurs within the laser pulse (resolution of 60 fs), indicating that the charge injection into TiO_2 occurs at the sub 15 fs timescale. This injection time is much faster than the hot electron lifetimes in GQDs (up to 10 ps) (Williams et al. 2013). Specifically, the hot electron lifetimes were found to increase as the GQD size is decreased and this behavior is explained by the "phonon bottleneck" effect, where the energy spacing in quantum-confined systems becomes larger than the phonon frequencies, resulting in the lower efficiency of relaxation of higher-energy excited states. Computational studies illustrated in Fig. 12b–e have explored the effect of GQD/TiO_2 bonding on the efficiency of electron transfer (Long et al. 2017). The covalent binding through carboxylate linker was found to lead to weak electronic coupling, while strong electronic coupling and ultrafast charge injection are predicted for the through-space π-electron adduct, pointing to the importance of van der Waals interactions in mediating fast charge separation.

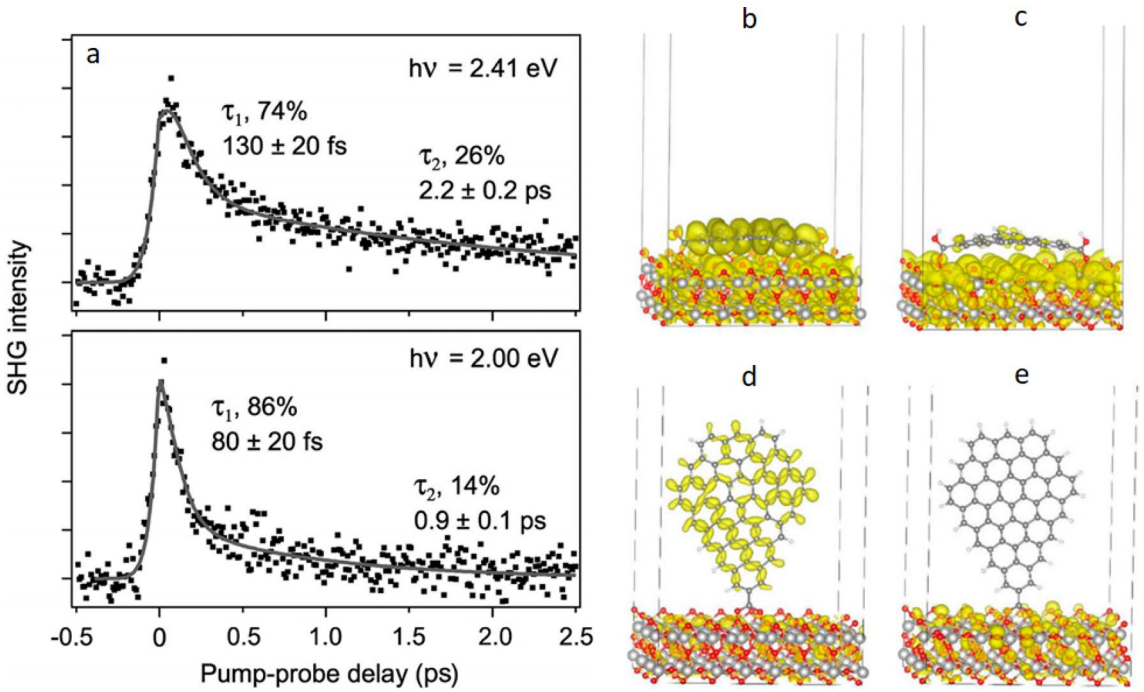

Fig. 12 **a** Photo-induced charge transfer dynamics observed via time-resolved SHG of GQD/TiO_2(110) at 300 K and pump energies of 2.41 eV (top) and 2.00 eV (bottom). Charge densities of photoexcited **b** donor state of F-coronene/TiO_2, **c** acceptor state of F-coronene/TiO_2, **d** donor sate of VGQD/TiO_2, and **e** acceptor state of VGQD/TiO_2 (Williams et al. 2013; Long et al. 2017)

Similar effects of GQD size on hot electron cooling rates was observed for GQD/MoS_2 hybrids (Fig. 13a) (Shan et al. 2019). In addition to the hot electron cooling dynamics, the rates of cold electron injection (τ_{cold}) and subsequent charge recombination (τ_{back}) were also found to depend on the GQD size. For example, Fig. 13b, c show that both τ_{cold} and τ_{back} increase with increased GQD size in GQD/MoS_2 hybrids, which was assigned to the change in the thermodynamic driving force for photoinduced electron transfer with the GQD size and was well modeled using Marcus theory.

Electron and energy transfer kinetics were also investigated for hybrids involving GQDs and transition metal complexes (Kim et al. 2006; Elliott et al. 2016; Umeyama et al. 2019; Singh et al. 2020a). For example, our group investigated the excited-state behavior of GQDs that contain cobaloxime-based hydrogen evolution catalysts shown in Fig. 14 (Singh et al. 2020a).We found that the excited state, localized on the GQD moiety, is readily quenched in the presence of cobaloximes. Our experimental results indicate that the quenching mechanism involves either the photoinduced electron transfer from photoexcited GQD to the cobaloxime or Dexter-type energy transfer. No charge-separated states were observed in transient absorption, indicating that the system quickly relaxes back to the ground state.

Applications

The highly tunable photophysical properties of nanographenes make them promising materials for light-emitting diode (LED) applications. Furthermore, the low cost and low toxicity of nanographenes, combined with their high thermal and photo-stability makes them ideal LED phosphors. For indoor lighting applications, warm LEDs are needed to minimize eye fatigue effects. Warm LEDs are made using UV-LEDs coated with broad-emission red, green and blue tricolor phosphors. Given that GQDs can be photoexcited in the UV-region and they tend to exhibit broad emission spectra, high PL QYs and tunable emission wavelengths, they have been successfully applied as blue, green and red phosphors for warm LED applications (Qu et al. 2016; Wang et al. 2017). For example, three GQD phosphors that emit in blue (with PL QY = 72%), green (PL QY = 71%) and red (PL QY = 50%) were used to fabricate warm LED with a luminous efficiency of 31.3 lmW^{-1} at 20 mA current (Wang et al. 2017). In other LED applications, such as displays, phosphors should exhibit narrow emission bands. Until recently, GQDs had limited performance in such devices, because of their broad emission characteristics. However, narrow emission profiles were obtained by careful control over the GQD chemistry

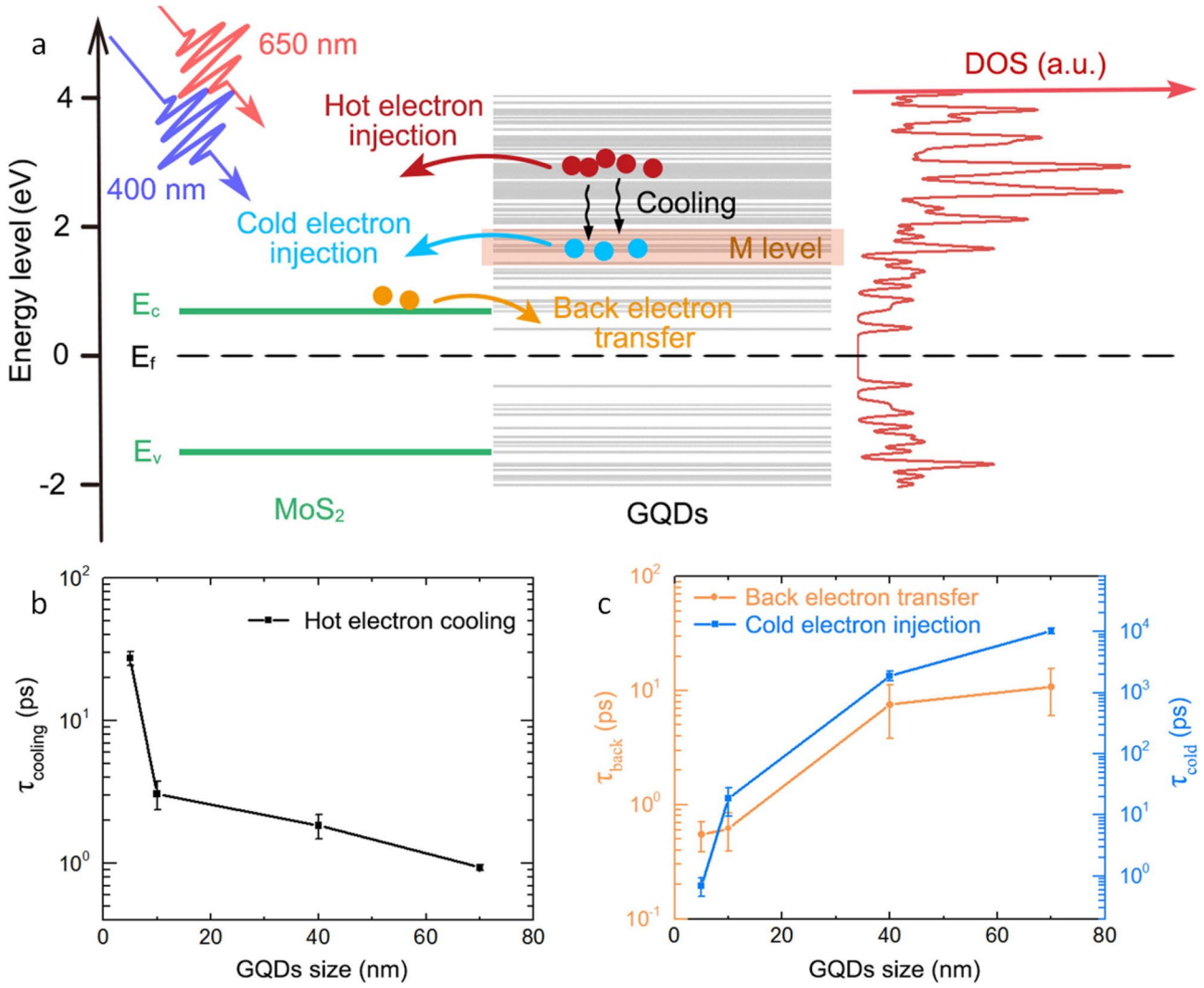

Fig. 13 **a** Band diagram of GQDs/MoS_2 heterostructure (left), calculated eigen states (middle), and density of states of GQDs (right). **b** Hot electron cooling lifetime for GQDs of varying size. **c** Lifetimes of cold electron injection and back electron transfer in heterostructures (Shan et al. 2019)

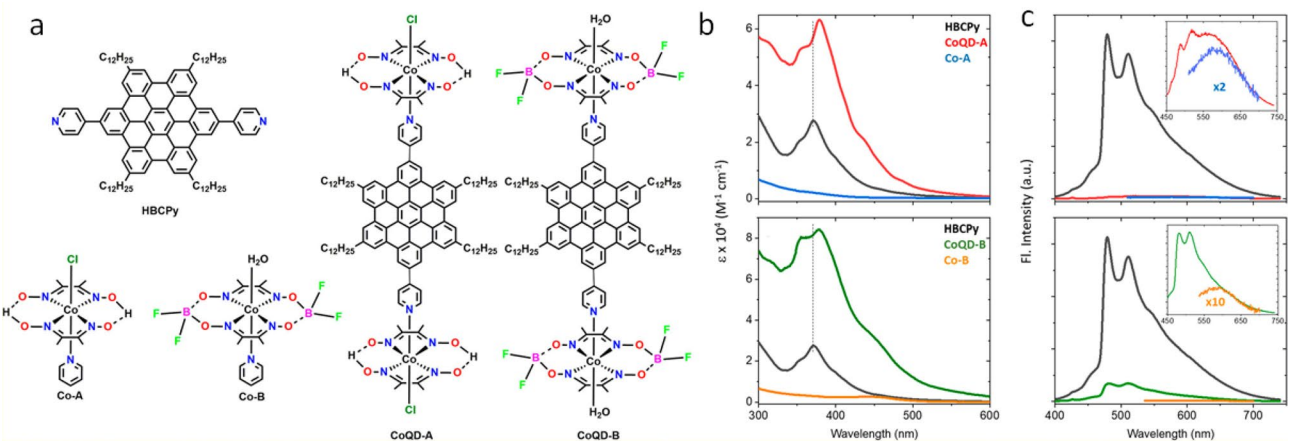

Fig. 14 **a** Structures of some cobaloxime-based hydrogen evolution catalysts. **b** Absorption and **c** emission spectra of the structures on the left, showing quenching on photoexcitation (Singh et al. 2020a)

(Yuan et al. 2018, 2020). For example, the presence of carboxylate groups on the edges of GQDs was found to cause the emission broadening due to the changes in the π-delocalization of the chromophores as the carboxylate group rotates in and out of plane of the nanographene. This paper reports first HBC based LED which shows electroluminescence peak at 490 nm with a FWHM of 20 nm. Amination of GQD edges to remove the carboxylate groups has produced deep-blue LEDs with 70% QY, among the highest QY values of GQDs to date and comparable to the highest performing Cd^{2+}/Pb^{2+}-based emitters (Yuan et al. 2020). In another study, an exceptional narrowband emission (FWHM = 30 nm) was achieved using T-GQDs, and highest QYs to date were reported (QY_{blue} = 66%, QY_{green} = 72%, QY_{yellow} = 62%, and QY_{red} = 54%, Fig. 15) (Yuan et al. 2020).

The impressive emissive properties of nanographenes make them promising contenders for low-threshold lasers with long operational times (Yuan et al. 2019b; Bonal et al. 2019; Zou et al. 2020) and optical sensors (Sun et al. 2013; Ananthanarayanan et al. 2014; Shi et al. 2015; Song et al. 2016; Hai et al. 2018; Xu et al. 2018). For example, T-GQDs in Au–Ag bimetallic porous nanowires have shown lasing application with performances superior than perovskites and traditional colloidal semiconductor QD based random lasers. The prepared blue, green and red random lasers showed a lasing threshold of 0.087, 0.052 and 0.048 mJ/cm^2 along with corresponding FWHMs of 0.9, 0.37 and 0.82 nm, respectively (Yuan et al. 2019b). Additionally, distribution feedback lasers based on zigzag-edged nanographenes have been demonstrated to operate at a threshold as low as 11 μJ/cm^2 with a narrow FWHM of 0.13 nm (Bonal et al. 2019). On the biological sensing front, functionalized GQDs allow binding with the target analyte through various kinds of interactions, such as electrostatic attraction or π–π conjugation, results in the quenching of PL (Hai et al. 2018). For example, chemically modified GQDs have been demonstrated to sense biological Fe^{3+} (Ananthanarayanan et al. 2014), Ni^{2+} (Xu et al. 2018), Cu^{2+} (Sun et al. 2013), and H^+ ions (Song et al. 2016). Challenges to be overcome in the biological application of nanographenes are being studied and include biocompatibility, selectivity, and cytotoxicity.

Nanographenes have been used as photoactive materials in photovoltaics with limited success (Qin et al. 2015). Due to high exciton binding energy of nanographene materials, photovoltaic nanographene cells are made as bulk heterojunctions with appropriate electron donors or acceptors. These blends ensure efficient charge separation at interfaces

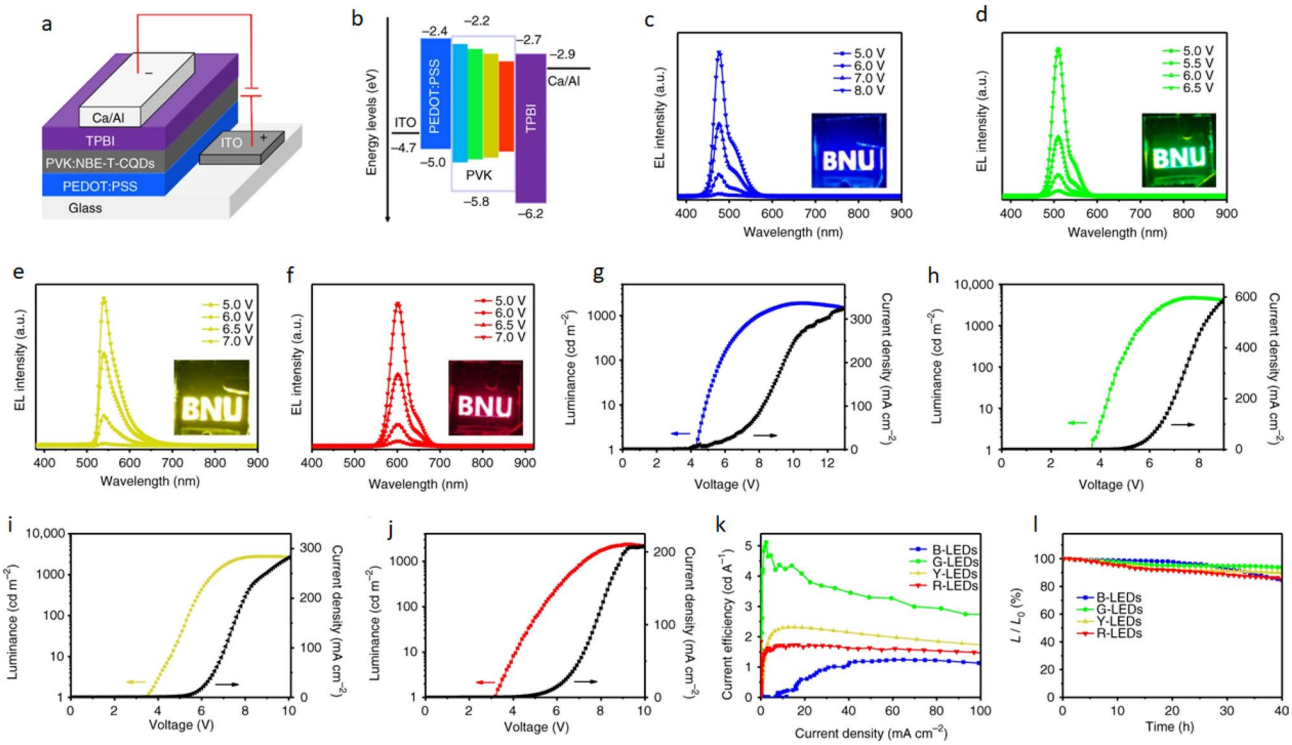

Fig. 15 **a** GQD-based LED device structure. **b** Energy level diagram of LED device. Electroluminescence of LEDs based on **c** blue, **d** green, **e** yellow, and **f** red emitting triangular GQDs at different bias voltages. Maximum luminance-current–voltage characteristic of **g** blue, **h** green, **i** yellow, **j** and red emitting triangular GQDs. **k** Current efficiency versus current density and **l** stability plots of the GQD-based LED devices (Yuan et al. 2018)

and 3–4% power conversion efficiencies can be achieved. Nanographenes have also been used as "photon management" chromophores for photovoltaic devices (Khan and Kim 2018). Namely, GQDs with large Stokes shifts and high PL QYs were utilized to down-covert blue photons for use in $Cu(In,Ga)Se_2$ solar cells. This conversion of blue photons to lower energy photons minimizes the efficiency loss associated with the parasitic absorption of blue light by ZnO and CdS windows and buffer layers in these devices. Furthermore, GQDs have been shown to uplift the Fermi level of perovskite-based films and improving the charge separation in them resulting in an increase of solar cell efficiency by 2.7% (Gan et al. 2019).

Nanographenes are also being developed for application in photocatalysis, such as solar water splitting and carbon dioxide reduction (Yan et al. 2018, 2020; Tsai et al. 2020). For example, efficient photoelectrochemical water splitting was achieved using 0D/2D van der Waals heterojunctions composed of zero-dimensional GQDs and two-dimensional graphene (Yan et al. 2020). The energy gap of GQDs was tuned to be ~ 2 eV to ensure the most efficient harvesting of the solar spectrum and sufficient energy to drive the water splitting. The performance of these heterojunctions in photoelectrochemical water splitting is shown in Fig. 16. The presence of several-fold current enhancement is observed under illumination, indicating efficient photocatalysis. The GQD-graphene hybrids in the aforementioned study exhibited a fast Volmer-Heyrovsky mechanism for hydrogen evolution and a fast two-step mechanism for oxygen evolution. The performance of GQDs in photocatalytic water splitting can be optimized via chemical tuning of the GQD. For example, Yan and coworkers demonstrated a systematic approach to engineering bandgaps in GQDs for photocatalytic water splitting and CO_2 reduction in 2018 (Yan et al. 2018). Incorporation of a Z-scheme mechanism was achieved using GQD materials modified via π-system extension to introduce either p- and n-type semiconducting domains. Upon excitation with visible light (420–800 nm), an electron is generated in the p-type domain (which reduces CO_2 to methanol) and a hole forms in the n-type domain (which oxidizes water to produce O_2). The authors note that, while the photocatalytic performance of their GQDs are not competitive with other common photocatalysts in industry (H_2 yield of 130 μmol h^{-1}, and methanol yield of 0.695 μmol h^{-1} $g_{cat}{}^{-1}$),

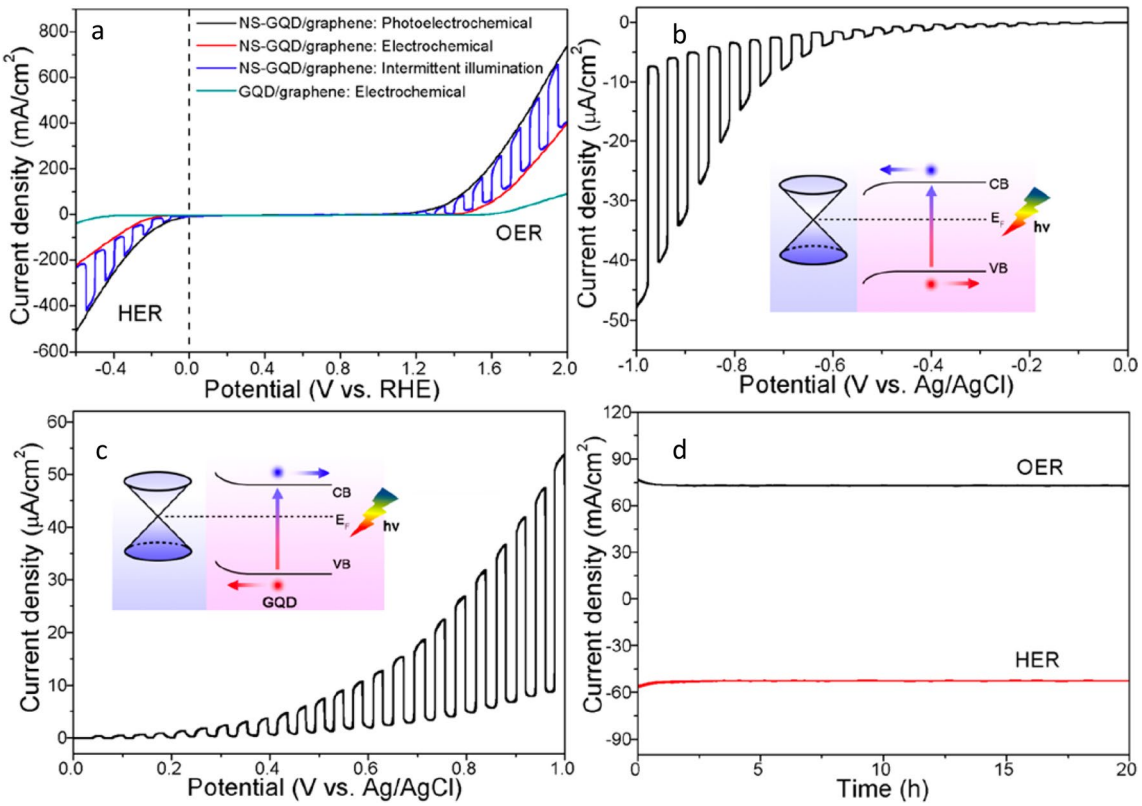

Fig. 16 Electro- and photoelectrochemical water splitting results of GQDs. **a** Hydrogen evolution and oxygen evolution linear scan curves of heteroatom nitrogen/sulfur-containing GQDs/graphene hybrid structures in 1.0 M KOH with Xe lamp illumination (black) intermittent illumination (blue), and with no illumination (red). For reference, electrochemical performance of GQD/graphene (green) is also shown. Cathodic **b** and anodic **c** current densities of NS-GQD/graphene in ethanol with 0.1 M KOH with intermittent illumination. **d** HER and OER current densities with respect to time under Xe lamp illumination (Lin et al. 2018) (Yan et al. 2020)

optimization of the GQD for photocatalysis is a necessary and important step towards synthesizing GQD-hybrid materials that exhibit competitive photocatalysis.

Future directions

Our short review summarizes a range of interesting photophysical properties of nanographenes and their applications in optoelectronic and photocatalytic applications. One particular area that has shown great promise, but has not been explored in great detail, is photocatalysis. With recent developments in bottom-up wet chemistry synthetic methods, photocatalytic nanographene materials can be readily made from GNRs or GQDs and molecular transition metal catalysts for water splitting, carbon dioxide reduction, or any other oxidation/reduction reaction. Tunable energy gaps of nanographenes, along with efficient exciton and charge carrier mobilities in these materials make them ideal platforms for photocatalysis. Furthermore, nanographenes can be solubilized using appropriate pendant groups, enabling "wireless" photocatalysis in solution. Future studies investigating structural factors that control light harvesting, photoinduced charge separation/recombination and subsequent bond forming and breaking steps will enable a new generation of nanographene photocatalysts.

Acknowledgements We acknowledge the support provided by the National Science Foundation (CHE-1806388 and CHE-1954298) and the U.S. Department of Energy (DOE), Office of Science, Office of Basic Energy Sciences, Division of Chemical Sciences, Geosciences and Biosciences, through Argonne National Laboratory under Contract No. DE-AC02-06CH11357.

Declarations

Conflict of interest The authors declare no competing financial interest.

References

Allen MJ, Tung VC, Kaner RB (2010) Honeycomb carbon: a review of graphene. Chem Rev 110:132–145. https://doi.org/10.1021/cr900070d

Ananthanarayanan A, Wang X, Routh P et al (2014) Facile synthesis of graphene quantum dots from 3D graphene and their application for Fe $^{3+}$ sensing. Adv Funct Mater 24:3021–3026. https://doi.org/10.1002/adfm.201303441

Bao L, Zhang Z-L, Tian Z-Q et al (2011) Electrochemical tuning of luminescent carbon nanodots: from preparation to luminescence mechanism. Adv Mater 23:5801–5806. https://doi.org/10.1002/adma.201102866

Bene JD, Jaffé HH (1968) Use of the CNDO method in spectroscopy. I. Benzene, pyridine, and the diazines. J Chem Phys 48:1807–1813. https://doi.org/10.1063/1.1668915

Berlman I (1971) Handbook of florescence spectra of aromatic molecules. Elsevier Science, Oxford

Bodenmann AK, MacDonald AH (2007) Graphene: exploring carbon flatland. Phys Today 60:35–41. https://doi.org/10.1063/1.2774096

Boens N, Qin W, Basarić N et al (2007) Fluorescence lifetime standards for time and frequency domain fluorescence spectroscopy. Anal Chem 79:2137–2149. https://doi.org/10.1021/ac062160k

Bonal V, Muñoz-Mármol R, Gordillo Gámez F et al (2019) Solution-processed nanographene distributed feedback lasers. Nat Commun 10:3327. https://doi.org/10.1038/s41467-019-11336-0

Bronner C, Gerbert D, Broska A, Tegeder P (2016) Excitonic states in narrow armchair graphene nanoribbons on gold surfaces. J Phys Chem C 120:26168–26172. https://doi.org/10.1021/acs.jpcc.6b10834

Bryson KL, Peeters Z, Salama F et al (2011) The ORGANIC experiment on EXPOSE-R on the ISS: flight sample preparation and ground control spectroscopy. Adv Space Res 48:1980–1996. https://doi.org/10.1016/j.asr.2011.07.017

Calabro RL, Yang D-S, Kim DY (2019) Controlled nitrogen doping of graphene quantum dots through laser ablation in aqueous solutions for photoluminescence and electrocatalytic applications. ACS Appl Nano Mater 2:6948–6959. https://doi.org/10.1021/acsanm.9b01433

Carlson LJ, Krauss TD (2008) Photophysics of individual single-walled carbon nanotubes. Acc Chem Res 41:235–243. https://doi.org/10.1021/ar700136v

Chen Z, Wang HI, Teyssandier J et al (2017) Chemical vapor deposition synthesis and terahertz photoconductivity of low-band-gap $n = 9$ armchair graphene nanoribbons. J Am Chem Soc 139:3635–3638. https://doi.org/10.1021/jacs.7b00776

Cho HJ, Kim SW, Kim S et al (2020) Suppressing π–π stacking interactions for enhanced solid-state emission of flat aromatic molecules via edge functionalization with picket-fence-type groups. J Mater Chem C. https://doi.org/10.1039/D0TC04376A

Clar E (1983) The Aromatic Sextet. In: Rondia D, Cooke M, Haroz RK (eds) Mobile source emissions including policyclic organic species. Springer, Dordrecht, pp 49–58

Cloke RR, Marangoni T, Nguyen GD et al (2015) Site-Specific substitutional boron doping of semiconducting armchair graphene nanoribbons. J Am Chem Soc 137:8872–8875. https://doi.org/10.1021/jacs.5b02523

Cudazzo P, Sottile F, Rubio A, Gatti M (2015) Exciton dispersion in molecular solids. J Phys Condens Matter. https://doi.org/10.1088/0953-8984/27/11/113204

Dai Y, Liu Y, Ding K, Yang J (2018) A short review of nanographenes: structures, properties and applications. Mol Phys 116:987–1002. https://doi.org/10.1080/00268976.2018.1433881

Deilmann T, Rohlfing M (2017) Huge trionic effects in graphene nanoribbons. Nano Lett 17:6833–6837. https://doi.org/10.1021/acs.nanolett.7b03111

Denk R, Hohage M, Zeppenfeld P et al (2014) Exciton-dominated optical response of ultra-narrow graphene nanoribbons. Nat Commun 5:4253. https://doi.org/10.1038/ncomms5253

Dou C, Saito S, Matsuo K et al (2012) A boron-containing PAH as a substructure of boron-doped graphene. Angew Chem Int Ed 51:12206–12210. https://doi.org/10.1002/anie.201206699

Dresselhaus MS, Dresselhaus G, Saito R, Jorio A (2007) Exciton photophysics of carbon nanotubes. Annu Rev Phys Chem 58:719–747. https://doi.org/10.1146/annurev.physchem.58.032806.104628

Dumslaff T, Yang B, Maghsoumi A et al (2016) Adding four extra K-regions to Hexa-*peri*-hexabenzocoronene. J Am Chem Soc 138:4726–4729. https://doi.org/10.1021/jacs.6b01976

Dumslaff T, Gu Y, Paternò GM et al (2020) Hexa- *peri* -benzocoronene with two extra K-regions in an *ortho* -configuration. Chem Sci. https://doi.org/10.1039/D0SC04649C

Elliott ABS, Horvath R, Sun X-Z et al (2016) Long-lived charge transfer excited states in HBC-polypyridyl complex hybrids. Inorg Chem 55:4710–4719. https://doi.org/10.1021/acs.inorgchem.5b02602

Gan X, Yang S, Zhang J et al (2019) Graphite-N doped graphene quantum dots as semiconductor additive in perovskite solar cells. ACS Appl Mater Interfaces 11:37796–37803. https://doi.org/10.1021/acsami.9b13375

Grimme S (2008) Do special noncovalent π–π stacking interactions really exist? Angew Chem Int Ed 47:3430–3434. https://doi.org/10.1002/anie.200705157

Hai X, Feng J, Chen X, Wang J (2018) Tuning the optical properties of graphene quantum dots for biosensing and bioimaging. J Mater Chem B 6:3219–3234. https://doi.org/10.1039/C8TB00428E

Han P, Yao X, Müllen K et al (2020) Size-dependent electron transfer from atomically defined nanographenes to metal oxide nanoparticles. Nanoscale 12:16046–16052. https://doi.org/10.1039/D0NR03891A

Harris DC, Bertolucci MD (1989) Symmetry and spectroscopy: an introduction to vibrational and electronic spectroscopy. Dover Publications, New York

Hestand NJ, Spano FC (2017) Molecular aggregate photophysics beyond the kasha model: novel design principles for organic materials. Acc Chem Res 50:341–350. https://doi.org/10.1021/acs.accounts.6b00576

Hong X, Posadas A, Zou K et al (2009) High-mobility few-layer graphene field effect transistors fabricated on epitaxial ferroelectric gate oxides. Phys Rev Lett. https://doi.org/10.1103/PhysRevLett.102.136808

Hu Y, Xie P, De Corato M et al (2018) Bandgap engineering of graphene nanoribbons by control over structural distortion. J Am Chem Soc 140:7803–7809. https://doi.org/10.1021/jacs.8b02209

Huang Y, Xu F, Ganzer L et al (2018) Intrinsic properties of single graphene nanoribbons in solution: synthetic and spectroscopic studies. J Am Chem Soc 140:10416–10420. https://doi.org/10.1021/jacs.8b06028

Ilic S, Zoric MR, Kadel UP et al (2017) Metal-free motifs for solar fuel applications. Annu Rev Phys Chem 68:305–331. https://doi.org/10.1146/annurev-physchem-052516-050924

Ivanov I, Hu Y, Osella S et al (2017) Role of edge engineering in photoconductivity of graphene nanoribbons. J Am Chem Soc 139:7982–7988. https://doi.org/10.1021/jacs.7b03467

Jensen SA, Ulbricht R, Narita A et al (2013) Ultrafast photoconductivity of graphene nanoribbons and carbon nanotubes. Nano Lett 13:5925–5930. https://doi.org/10.1021/nl402978s

Ji Z, Dervishi E, Doorn SK, Sykora M (2019) Size-dependent electronic properties of uniform ensembles of strongly confined graphene quantum dots. J Phys Chem Lett 10:953–959. https://doi.org/10.1021/acs.jpclett.9b00119

Jorio A, Saito R, Hertel T et al (2004) Carbon nanotube photophysics. MRS Bull 29:276–280. https://doi.org/10.1557/mrs2004.80

Kastler M, Schmidt J, Pisula W et al (2006) From armchair to zigzag peripheries in nanographenes. J Am Chem Soc 128:9526–9534. https://doi.org/10.1021/ja062026h

Kaufmann C, Kim W, Nowak-Król A et al (2018) Ultrafast exciton delocalization, localization, and excimer formation dynamics in a highly defined perylene bisimide quadruple π-stack. J Am Chem Soc 140:4253–4258. https://doi.org/10.1021/jacs.7b11571

Kawai S, Saito S, Osumi S et al (2015) Atomically controlled substitutional boron-doping of graphene nanoribbons. Nat Commun 6:8098. https://doi.org/10.1038/ncomms9098

Kawai S, Nakatsuka S, Hatakeyama T et al (2018) Multiple heteroatom substitution to graphene nanoribbon. Sci Adv. https://doi.org/10.1126/sciadv.aar7181

Keerthi A, Hou IC-Y, Marszalek T et al (2016) Hexa- *peri* -hexabenzocoronene with different acceptor units for tuning optoelectronic properties. Chem Asian J 11:2710–2714. https://doi.org/10.1002/asia.201600638

Khan F, Kim JH (2018) N-functionalized graphene quantum dots with ultrahigh quantum yield and large stokes shift: efficient down-converters for CIGS solar cells. ACS Photonics 5:4637–4643. https://doi.org/10.1021/acsphotonics.8b01125

Kim K-Y, Liu S, Köse ME, Schanze KS (2006) Photophysics of platinum−acetylide substituted hexa- *peri* -hexabenzocoronenes. Inorg Chem 45:2509–2519. https://doi.org/10.1021/ic051788v

Li L, Yan X (2010) Colloidal graphene quantum dots. J Phys Chem Lett 1:2572–2576. https://doi.org/10.1021/jz100862f

Li X, Rui M, Song J et al (2015a) Carbon and graphene quantum dots for optoelectronic and energy devices: a review. Adv Funct Mater 25:4929–4947. https://doi.org/10.1002/adfm.201501250

Li Y, Shu H, Niu X, Wang J (2015b) Electronic and optical properties of edge-functionalized graphene quantum dots and the underlying mechanism. J Phys Chem C 119:24950–24957. https://doi.org/10.1021/acs.jpcc.5b05935

Li Y, Shu H, Wang S, Wang J (2015c) Electronic and optical properties of graphene quantum dots: the role of many-body effects. J Phys Chem C 119:4983–4989. https://doi.org/10.1021/jp506969r

Lim S-H, Bjorklund TG, Spano FC, Bardeen CJ (2004) Exciton delocalization and superradiance in tetracene thin films and nanoaggregates. Phys Rev Lett. https://doi.org/10.1103/PhysRevLett.92.107402

Lin JDA, Mikhnenko OV, Chen J et al (2014) Systematic study of exciton diffusion length in organic semiconductors by six experimental methods. Mater Horiz 1:280–285. https://doi.org/10.1039/C3MH00089C

Long R, Casanova D, Fang W-H, Prezhdo OV (2017) Donor-acceptor interaction determines the mechanism of photoinduced electron injection from graphene quantum dots into TiO_2: π-stacking supersedes covalent bonding. J Am Chem Soc 139:2619–2629. https://doi.org/10.1021/jacs.6b09598

Majewski MA, Stępień M (2019) Bowls, hoops, and saddles: synthetic approaches to curved aromatic molecules. Angew Chem Int Ed 58:86–116. https://doi.org/10.1002/anie.201807004

Manga KK, Zhou Y, Yan Y, Loh KP (2009) Multilayer hybrid films consisting of alternating graphene and titania nanosheets with ultrafast electron transfer and photoconversion properties. Adv Funct Mater 19:3638–3643. https://doi.org/10.1002/adfm.200900891

Marciniak H, Li X-Q, Würthner F, Lochbrunner S (2011) One-dimensional exciton diffusion in perylene bisimide aggregates. J Phys Chem A 115:648–654. https://doi.org/10.1021/jp107407p

Martinez CR, Iverson BL (2012) Rethinking the term "pi-stacking." Chem Sci 3:2191. https://doi.org/10.1039/c2sc20045g

Miyauchi Y (2013) Photoluminescence studies on exciton photophysics in carbon nanotubes. J Mater Chem C 1:6499. https://doi.org/10.1039/c3tc00947e

Morozov SV, Novoselov KS, Katsnelson MI et al (2008) Giant intrinsic carrier mobilities in graphene and its bilayer. Phys Rev Lett. https://doi.org/10.1103/PhysRevLett.100.016602

Mueller ML, Yan X, McGuire JA, Li L (2010) Triplet states and electronic relaxation in photoexcited graphene quantum dots. Nano Lett 10:2679–2682. https://doi.org/10.1021/nl101474d

Nakajima A (1973) Fluorescence lifetime of pyrene in different solvents. Bull Chem Soc Jpn 46:2602–2604. https://doi.org/10.1246/bcsj.46.2602

Narita A, Feng X, Hernandez Y et al (2014) Synthesis of structurally well-defined and liquid-phase-processable graphene

nanoribbons. Nat Chem 6:126–132. https://doi.org/10.1038/nchem.1819
Narita A, Wang X-Y, Feng X, Müllen K (2015) New advances in nanographene chemistry. Chem Soc Rev 44:6616–6643. https://doi.org/10.1039/C5CS00183H
Olaya-Castro A, Scholes GD (2011) Energy transfer from Förster-Dexter theory to quantum coherent light-harvesting. Int Rev Phys Chem 30:49–77. https://doi.org/10.1080/0144235X.2010.537060
Paternò GM, Chen Q, Wang X-Y et al (2017) Synthesis of dibenzo[*hi, st*]ovalene and its amplified spontaneous emission in a polystyrene matrix. Angew Chem Int Ed 56:6753–6757. https://doi.org/10.1002/anie.201700730
Pramanik A, Biswas S, Tiwary CS et al (2020) Forster resonance energy transfer assisted white light generation and luminescence tuning in a colloidal graphene quantum dot-dye system. J Colloid Interface Sci 565:326–336. https://doi.org/10.1016/j.jcis.2020.01.019
Qin Y, Cheng Y, Jiang L et al (2015) Top-down strategy toward versatile graphene quantum dots for organic/inorganic hybrid solar cells. ACS Sustain Chem Eng 3:637–644. https://doi.org/10.1021/sc500761n
Qu S, Zhou D, Li D et al (2016) Toward efficient orange emissive carbon nanodots through conjugated sp^2—domain controlling and surface charges engineering. Adv Mater 28:3516–3521. https://doi.org/10.1002/adma.201504891
Rieger R, Müllen K (2010) Forever young: polycyclic aromatic hydrocarbons as model cases for structural and optical studies. J Phys Org Chem N/a-N/a. https://doi.org/10.1002/poc.1644
Scholes GD, Rumbles G (2006) Excitons in nanoscale systems. Nat Mater 5:683–696. https://doi.org/10.1038/nmat1710
Segawa Y, Ito H, Itami K (2016) Structurally uniform and atomically precise carbon nanostructures. Nat Rev Mater 1:15002. https://doi.org/10.1038/natrevmats.2015.2
Shan H, Yu Y, Zhang R et al (2019) Electron transfer and cascade relaxation dynamics of graphene quantum dots/MoS2 monolayer mixed-dimensional van der Waals heterostructures. Mater Today 24:10–16. https://doi.org/10.1016/j.mattod.2019.01.015
Shi J, Chan C, Pang Y et al (2015) A fluorescence resonance energy transfer (FRET) biosensor based on graphene quantum dots (GQDs) and gold nanoparticles (AuNPs) for the detection of mecA gene sequence of Staphylococcus aureus. Biosens Bioelectron 67:595–600. https://doi.org/10.1016/j.bios.2014.09.059
Singh V, Gupta N, Hargenrader GN et al (2020a) Photophysics of graphene quantum dot assemblies with axially coordinated cobaloxime catalysts. J Chem Phys. https://doi.org/10.1063/5.0018581
Singh V, Zoric MR, Hargenrader GN et al (2020b) Exciton coherence length and dynamics in graphene quantum dot assemblies. J Phys Chem Lett 11:210–216. https://doi.org/10.1021/acs.jpclett.9b03384
Soavi G, Dal Conte S, Manzoni C et al (2016a) Exciton–exciton annihilation and biexciton stimulated emission in graphene nanoribbons. Nat Commun 7:11010. https://doi.org/10.1038/ncomms11010
Soavi G, Scotognella F, Lanzani G, Cerullo G (2016b) Ultrafast photophysics of single-walled carbon nanotubes. Adv Opt Mater 4:1670–1688. https://doi.org/10.1002/adom.201600361
Solà M (2013) Forty years of Clar's aromatic π-sextet rule. Front Chem. https://doi.org/10.3389/fchem.2013.00022
Son Y-W, Cohen ML, Louie SG (2006) Energy gaps in graphene nanoribbons. Phys Rev Lett. https://doi.org/10.1103/PhysRevLett.97.216803
Song S-H, Jang M, Yoon H et al (2016) Size and pH dependent photoluminescence of graphene quantum dots with low oxygen content. RSC Adv 6:97990–97994. https://doi.org/10.1039/C6RA21651J
Spano FC, Yamagata H (2011) Vibronic coupling in J-aggregates and beyond: a direct means of determining the exciton coherence length from the photoluminescence spectrum. J Phys Chem B 115:5133–5143. https://doi.org/10.1021/jp104752k
Stępień M, Gońka E, Żyła M, Sprutta N (2017) Heterocyclic nanographenes and other polycyclic heteroaromatic compounds: synthetic routes, properties, and applications. Chem Rev 117:3479–3716. https://doi.org/10.1021/acs.chemrev.6b00076
Sun H, Gao N, Wu L et al (2013) Highly photoluminescent amino-functionalized graphene quantum dots used for sensing copper ions. Chem - Eur J 19:13362–13368. https://doi.org/10.1002/chem.201302268
Sun C, Figge F, Ozfidan I et al (2015) Biexciton binding of dirac fermions confined in colloidal graphene quantum dots. Nano Lett 15:5472–5476. https://doi.org/10.1021/acs.nanolett.5b01888
Sung J, Kim P, Fimmel B et al (2015) Direct observation of ultrafast coherent exciton dynamics in helical π-stacks of self-assembled perylene bisimides. Nat Commun 6:8646. https://doi.org/10.1038/ncomms9646
Talrose, Stern E, Goncharova A, et al (2020) NIST chemistry webbook.
Tang Q, Zhou Z, Chen Z (2013) Graphene-related nanomaterials: tuning properties by functionalization. Nanoscale 5:4541. https://doi.org/10.1039/c3nr33218g
Tries A, Osella S, Zhang P et al (2020) Experimental observation of strong exciton effects in graphene nanoribbons. Nano Lett 20:2993–3002. https://doi.org/10.1021/acs.nanolett.9b04816
Tsai K-A, Hsieh P-Y, Lai T-H et al (2020) Nitrogen-doped graphene quantum dots for remarkable solar hydrogen production. ACS Appl Energy Mater 3:5322–5332. https://doi.org/10.1021/acsaem.0c00335
Turro NJ, Ramamurthy V, Scaiano JC (2009) Principles of molecular photochemistry: an introduction. University Science Books, Sausalito, Calif
Umeyama T, Hanaoka T, Yamada H et al (2019) Exclusive occurrence of photoinduced energy transfer and switching of its direction by rectangular π-extension of nanographenes. Chem Sci 10:6642–6650. https://doi.org/10.1039/C9SC01538H
Wang J, Cao S, Ding Y et al (2016) Theoretical investigations of optical origins of fluorescent graphene quantum dots. Sci Rep 6:24850. https://doi.org/10.1038/srep24850
Wang Z, Yuan F, Li X et al (2017) 53% efficient red emissive carbon quantum dots for high color rendering and stable warm white-light-emitting diodes. Adv Mater 29:1702910. https://doi.org/10.1002/adma.201702910
Wang X-Y, Yao X, Narita A, Müllen K (2019) Heteroatom-doped nanographenes with structural precision. Acc Chem Res 52:2491–2505. https://doi.org/10.1021/acs.accounts.9b00322
Wang X, Zhang X, Gu X et al (2020) A bright and stable violet carbon dot light-emitting diode. Adv Opt Mater 8:2000239. https://doi.org/10.1002/adom.202000239
Watson MD, Fechtenkötter A, Müllen K (2001) Big is beautiful−"aromaticity" revisited from the viewpoint of macromolecular and supramolecular benzene chemistry. Chem Rev 101:1267–1300. https://doi.org/10.1021/cr990322p
West BA, Womick JM, McNeil LE et al (2010) Ultrafast dynamics of frenkel excitons in tetracene and rubrene single crystals. J Phys Chem C 114:10580–10591. https://doi.org/10.1021/jp101621v
West BA, Womick JM, McNeil LE et al (2011) Influence of vibronic coupling on band structure and exciton self-trapping in α-perylene. J Phys Chem B 115:5157–5167. https://doi.org/10.1021/jp105115n
Williams KJ, Nelson CA, Yan X et al (2013) Hot electron injection from graphene quantum dots to TiO_2. ACS Nano 7:1388–1394. https://doi.org/10.1021/nn305080c

Xu A, He P, Huang T et al (2018) Selective supramolecular interaction of ethylenediamine functionalized graphene quantum dots: ultra-sensitive photoluminescence detection for nickel ion in vitro. Synth Met 244:106–112. https://doi.org/10.1016/j.synthmet.2018.05.013

Xu F, Yu C, Tries A et al (2019) Tunable superstructures of dendronized graphene nanoribbons in liquid phase. J Am Chem Soc 141:10972–10977. https://doi.org/10.1021/jacs.9b04927

Yamagata H, Maxwell DS, Fan J et al (2014) HJ-aggregate behavior of crystalline 7,8,15,16-tetraazaterrylene: introducing a new design paradigm for organic materials. J Phys Chem C 118:28842–28854. https://doi.org/10.1021/jp509011u

Yamijala SSRKC, Mukhopadhyay M, Pati SK (2015) Linear and nonlinear optical properties of graphene quantum dots: a computational study. J Phys Chem C 119:12079–12087. https://doi.org/10.1021/acs.jpcc.5b03531

Yan X, Li B, Cui X et al (2011) Independent tuning of the band gap and redox potential of graphene quantum dots. J Phys Chem Lett 2:1119–1124. https://doi.org/10.1021/jz200450r

Yan Y, Chen J, Li N et al (2018) Systematic bandgap engineering of graphene quantum dots and applications for photocatalytic water splitting and CO_2 reduction. ACS Nano 12:3523–3532. https://doi.org/10.1021/acsnano.8b00498

Yan Y, Zhai D, Liu Y et al (2020) van der Waals heterojunction between a bottom-up grown doped graphene quantum dot and graphene for photoelectrochemical water splitting. ACS Nano 14:1185–1195. https://doi.org/10.1021/acsnano.9b09554

Yano Y, Mitoma N, Ito H, Itami K (2020) A quest for structurally uniform graphene nanoribbons: synthesis, properties, and applications. J Org Chem 85:4–33. https://doi.org/10.1021/acs.joc.9b02814

Yu J, Park J, Van Wyk A et al (2018) Excited-state electronic properties in zr-based metal-organic frameworks as a function of a topological network. J Am Chem Soc 140:10488–10496. https://doi.org/10.1021/jacs.8b04980

Yuan F, Yuan T, Sui L et al (2018) Engineering triangular carbon quantum dots with unprecedented narrow bandwidth emission for multicolored LEDs. Nat Commun 9:2249. https://doi.org/10.1038/s41467-018-04635-5

Yuan F, He P, Xi Z et al (2019a) Highly efficient and stable white LEDs based on pure red narrow bandwidth emission triangular carbon quantum dots for wide-color gamut backlight displays. Nano Res 12:1669–1674. https://doi.org/10.1007/s12274-019-2420-x

Yuan F, Xi Z, Shi X et al (2019b) Ultrastable and low-threshold random lasing from narrow-bandwidth-emission triangular carbon quantum dots. Adv Opt Mater 7:1801202. https://doi.org/10.1002/adom.201801202

Yuan F, Wang Y-K, Sharma G et al (2020) Bright high-colour-purity deep-blue carbon dot light-emitting diodes via efficient edge amination. Nat Photonics 14:171–176. https://doi.org/10.1038/s41566-019-0557-5

Zhang ZZ, Chang K, Peeters FM (2008) Tuning of energy levels and optical properties of graphene quantum dots. Phys Rev B. https://doi.org/10.1103/PhysRevB.77.235411

Zhang W, Jin W, Fukushima T et al (2011) Supramolecular linear heterojunction composed of graphite-like semiconducting nanotubular segments. Science 334:340–343. https://doi.org/10.1126/science.1210369

Zhang Q, Jie J, Diao S et al (2015) Solution-processed graphene quantum dot deep-UV photodetectors. ACS Nano 9:1561–1570. https://doi.org/10.1021/acsnano.5b00437

Zhao S, Lavie J, Rondin L et al (2018) Single photon emission from graphene quantum dots at room temperature. Nat Commun 9:3470. https://doi.org/10.1038/s41467-018-05888-w

Zhao K, Zheng X, Zhang H et al (2019) Multi-color fluorescent carbon dots with single wavelength excitation for white light-emitting diodes. J Alloys Compd 793:613–619. https://doi.org/10.1016/j.jallcom.2019.04.146

Zhu X, Su H (2011) Scaling of excitons in graphene nanoribbons with armchair shaped edges. J Phys Chem A 115:11998–12003. https://doi.org/10.1021/jp202787h

Zhu J, German R, Senkovskiy BV et al (2018) Exciton and phonon dynamics in highly aligned 7-atom wide armchair graphene nanoribbons as seen by time-resolved spontaneous Raman scattering. Nanoscale 10:17975–17982. https://doi.org/10.1039/C8NR05950K

Zou Y, Bonal V, Moles Quintero S et al (2020) Perylene-fused, aggregation-free polycyclic aromatic hydrocarbons for solution-processed distributed feedback lasers. Angew Chem Int Ed 59:14927–14934. https://doi.org/10.1002/anie.202004789